

Alma Mater Studiorum Università di Bologna
Archivio istituzionale della ricerca

Polyphase post-Variscan thinning of the North Pyrenean crust: Constraints from the P-T-t-deformation history of the exhumed Variscan lower crust (Saleix Massif, France)

This is the final peer-reviewed author's accepted manuscript (postprint) of the following publication:

Published Version:

Asti, R., Rossetti, F., Lucci, F., Poujol, M., Lagabrielle, Y. (2021). Polyphase post-Variscan thinning of the North Pyrenean crust: Constraints from the P-T-t-deformation history of the exhumed Variscan lower crust (Saleix Massif, France). *TECTONOPHYSICS*, 820(229122), 1-18 [10.1016/j.tecto.2021.229122].

Availability:

This version is available at: <https://hdl.handle.net/11585/943169> since: 2023-10-03

Published:

DOI: <http://doi.org/10.1016/j.tecto.2021.229122>

Terms of use:

Some rights reserved. The terms and conditions for the reuse of this version of the manuscript are specified in the publishing policy. For all terms of use and more information see the publisher's website.

This item was downloaded from IRIS Università di Bologna (<https://cris.unibo.it/>).
When citing, please refer to the published version.

(Article begins on next page)

This is the final peer-reviewed accepted manuscript of:

Asti, R; Rossetti, F; Lucci, F; Poujol, M; Lagabriele, Y: *Polyphase post-Variscan thinning of the North Pyrenean crust: Constraints from the P-T-t-deformation history of the exhumed Variscan lower crust (Saleix Massif, France)*

TECTONOPHYSICS vol. 820 ISSN 0040-1951

DOI: 10.1016/j.tecto.2021.229122

The final published version is available online at:

<https://dx.doi.org/10.1016/j.tecto.2021.229122>

Terms of use:

Some rights reserved. The terms and conditions for the reuse of this version of the manuscript are specified in the publishing policy. For all terms of use and more information see the publisher's website.

This item was downloaded from IRIS Università di Bologna (<https://cris.unibo.it/>)

When citing, please refer to the published version.

Polyphase post-Variscan thinning of the North Pyrenean crust: Constraints from the P-T-t-deformation history of the exhumed Variscan lower crust (Saleix Massif, France)

Riccardo Asti^{1,2,1,*} riccardo.asti@geoazur.unice.fr, Federico Rossetti³, Federico Lucci³, Marc Poujol², Yves Lagabrielle²

¹Université Côte d'Azur, CNRS, Observatoire de la Côte d'Azur, IRD, Géoazur, France

²Univ Rennes, CNRS, Géosciences Rennes, UMR 6118, 35000 Rennes, France

³Dipartimento di Scienze, Sez. Scienze Geologiche, Università Roma Tre, Largo S. L. Murialdo 1, 00146 Rome, Italy

*Corresponding author.

Abstract

As part of the Variscan orogen, the Pyrenean realm has undergone several rifting episodes, starting from the Permian-Carboniferous post-orogenic collapse and culminating with mid-Cretaceous lithospheric mantle exhumation. We present the Pressure-Temperature-time-deformation (*P-T-t-d*) evolution of the tonalite bodies (here described for the first time) intruded in the late Carboniferous high pressure (HP) granulites of the Saleix Complex, forming the inner envelope of the Lherz peridotites (Aulus Basin, Ariège, France), that is used as a proxy to reconstruct the post-Hercynian evolution of the Pyrenean continental crust. By integrating textural investigations with metamorphic thermobarometry, and zircon and titanite U-Pb geochronology, we (i) constrain timing and thermo-baric conditions related to the transition from magma emplacement to solid-state syn-tectonic deformation in tonalite(s); and (ii) discuss implications on the polyphase exhumation history of the granulite host rocks. Emplacement of the Saleix tonalite(s) took place in the early Permian

¹ Postal address: UMR Géoazur - Campus Azur du CNRS 250 rue Albert Einstein - CS 10269 - F 06905 SOPHIA ANTIPOLIS Cedex, France

(ca. 281 Ma), in a thermo-baric environment ($P = 0.5 \pm 0.1$ GPa and $T = 750-880 \pm 20$ °C) attesting for an important thinning of the Pyrenean crust at the end of the Variscan cycle. Solid-state deformation occurred during the mid-Cretaceous (ca. 96 Ma), at shallow crustal depths (≤ 10 km) and under amphibolite facies metamorphic conditions. These results document that rifting events had already thinned the Pyrenean crust prior to the Cretaceous mantle exhumation and that the lower crust was affected by ductile deformation during the Cretaceous rifting. Our study demonstrates that in the Pyrenean realm the Permian crustal thinning played a very important role and that mantle exhumation resulted from polyphase post-Variscan, Permian-to-Cretaceous crustal thinning episodes.

Keywords: European Variscides; Continental rifting; Petrochronology; Pyrenees

1. Introduction

The European Variscides recorded polyphase (late Paleozoic to Mesozoic) post-orogenic lithosphere thinning during rifting, break-up and fragmentation of the Pangea supercontinent (e.g. Burg *et al.* 1994; Ziegler & Dèzes, 2006 and references therein). Although definition of the thermal and rheological properties of the Variscan continental crust is relevant for understanding the space-time evolution and the modes through which extensional tectonics operated in space and time, few constraints exist in the literature regarding the pre-rifting crustal structure (e.g. Espurt *et al.* 2019 and references therein).

As part of the former Carboniferous foreland basin of the European Variscan belt (e.g. Autran *et al.* 1995; Matte, 2001), the Pyrenean realm (Fig. 1) has experienced limited crustal thickening during orogenic construction (de Saint Blanquat *et al.* 1990; de Saint Blanquat 1993; Azambre & Guitard, 2001; de Hoym de Marien *et al.* 2019). Extensional tectonics started in Permian times (e.g. Bixel & Lucas, 1983; Vissers, 1992; Saspiturry *et al.* 2019), while some parts of the Variscan Pyrenees were possibly still experiencing transpressional tectonics (Denèle *et al.*, 2014; Cochelin *et al.* 2018; Lemirre *et al.*, 2019), and continued throughout the Mesozoic with several distinct rifting episodes (e.g. Puigdefabregas & Souquet, 1986; Barnolas & Chiron, 1995; Vergés & García-Senz, 2001; Vergés

et al. 2002). The understanding of the polyphase post-Variscan evolution of the Pyrenean continental crust may therefore bear important implications on the long-term evolution of the Iberia/Eurasia plate boundary. As a matter of fact, the Permian-Mesozoic configuration of the Pyrenean crust played a crucial role first in determining the structural and thermal evolution of the region during the Cretaceous rifting (Duretz *et al.* 2019; Lagabriele *et al.* 2020; Saspiturry *et al.*, 2021) and, subsequently, controlling the style and modes of tectonic re-activation during the Alpine crustal shortening (e.g. Jourdon *et al.* 2019 and references therein).

In the last decade, several studies focused on the mechanisms and timing of lithospheric thinning and mantle exhumation in the Pyrenean realm during the Cretaceous (Fig. 2) (e.g. Jammes *et al.* 2009; Lagabriele *et al.* 2010; Clerc & Lagabriele, 2014; Masini *et al.* 2014; Tugend *et al.* 2014; Clerc *et al.* 2015, 2016; Corre *et al.* 2016, 2018; de Saint Blanquat *et al.* 2016; Teixell *et al.* 2018; Asti *et al.* 2019; Saspiturry *et al.*, 2020). However, few information is available on the pre-Cretaceous inherited structure and thickness of the continental crust in the region (e.g. Asti *et al.* 2019 and references therein). The Pyrenean realm thus provides an excellent case study to understand the impact of Variscan inheritance on the Alpine tectonic evolution.

In order to bring new constraints on the polyphase tectono-metamorphic evolution of the continental crust in the Pyrenean realm in post-Variscan times, we conducted a petrochronological study on Permian tonalite intrusives emplaced in the Variscan lower crustal envelope of the Lherz peridotite (Aulus basin, France) (Fig. 2). We combined field work, micro-scale studies, multi-equilibrium thermobarometry and zircon and titanite U-Pb geochronology to define the Pressure-Temperature-time-deformation (*P-T-t-d*) evolution of the tonalites that is used to refine the exhumation history of the Variscan crust (host rocks). The results allow to define an alternative model for the polyphase post-Variscan thinning of the Pyrenean continental crust, culminating with lithospheric mantle exhumation during the mid-Cretaceous rifting.

2. Geological setting

The Pyrenean belt resulted from the convergence between the Iberian and the Eurasian plates between the Santonian and the Oligocene (Roure *et al.* 1989; Muñoz, 1992; Ford *et al.* 2016). The belt is classically subdivided in three distinct structural domains (from north to south; Choukroune, 1976; Fig. 2a): (i) the North Pyrenean Zone, which is delimited by the North Pyrenean Frontal Thrust to the north and by the North Pyrenean Fault to the south, which conventionally marks the boundary between the Iberian and the European plates; (ii) the prominent Axial Zone, which is characterized by the exposure of the Pyrenean Variscan basement; and (iii) the South Pyrenean Zone, which is enclosed between the Axial Zone to the north and the South Pyrenean Frontal Thrust to the south.

Continental collision followed the tectonic inversion of a former mid-Cretaceous oblique rifted domain which resulted in the opening of a series of pull apart/transensional basins (e.g. Choukroune & Mattauer, 1978; Debross, 1987, 1990) in response to the eastward drift of the Iberian plate with respect to the Eurasian plate (e.g. Olivet, 1996; Nirrengarten *et al.* 2018). The Cretaceous rifting resulted in severe crustal thinning that led to widespread sub-continental mantle exhumation in the Pyrenean realm, which is testified by several ultramafic bodies exposed in the North Pyrenean Zone (Monchoux, 1970; Fabriès *et al.* 1991, 1998; Lagabrielle *et al.* 2010; Saint-Blanquat *et al.* 2016; Fig. 2a). A well-known syn-extensional mid-Cretaceous HT-LP metamorphic event involved the pre-rift and the lowermost syn-rift successions that are spatially associated with the exhumed mantle in the North Pyrenean Zone (Albarède & Michard-Vitrac, 1978; Montigny *et al.* 1986; Golberg, 1987; Golberg & Maluski, 1988; Golberg & Leyreloup, 1990; Clerc & Lagabrielle, 2014; Clerc *et al.* 2015). Most of this metamorphism occurred in an E-W trending corridor known as Internal Metamorphic Zone, which is enclosed between the North Pyrenean Fault (to the south) and some Paleozoic massifs (to the north), known as North Pyrenean Massifs (Fig. 2a). These massifs have preserved the record of the entire history of the Variscan events, from the syn-orogenic moderate thickening, to the pervasive LP-HT metamorphism and associated magmatism, and finally, the late- (to post- ?) orogenic Permo-Carboniferous crustal thinning (e.g. de Saint Blanquat *et al.* 1990; Bouhallier *et al.* 1991; de Saint Blanquat, 1993).

The study area for this work is located on the southern margin of the Aulus basin (Fig. 2b). This basin is part of a series of sedimentary basins that developed between the Iberian and Eurasian plates during the mid-Cretaceous rifting and is located within the Internal

Metamorphic Zone. It is bounded to the north by the Trois Seigneurs North Pyrenean Massif and to the south of the North Pyrenean Fault. In the central part of the basin, several ultramafic bodies are exposed within the metamorphosed pre-rift Mesozoic series, among which the world-famous Etang de Lers (or Lherz) ultramafic body, which represents the lherzolite type locality.

Several granulitic basement units are known in the North Pyrenean Zone, particularly in some North Pyrenean Massifs (e.g. Agly, Castillon, Saint Barthélémy and Bessède de Sault massifs), in the Basque Ursuya massif and at the northern and southern margins of the Aulus basin. Most of the Pyrenean granulites were equilibrated at relatively low pressure conditions (with estimates ranging 0.4-0.6 GPa; e.g. Vielzeuf, 1980a, 1984; Andrieux 1982, de Saint Blanquat *et al.* 1990, Lemirre 2018; Siron *et al.* 2020) during late-Variscan times (Vielzeuf & Kornprobst, 1984; Delaperrière *et al.* 1994; Olivier *et al.* 2008; Lemirre 2018; Siron *et al.* 2020). In the Aulus basin, three main lenses of granulites crop out, two along the northern margin (*Les Plagnaux* and *Port de Lers*) and one on the southern margin (*Port de Saleix*) (Azambre & Ravier, 1978) (Fig. 2b). The highest pressures conditions known for the Pyrenean granulites (0.7-0.9 GPa, with most of the values ranging around 0.7 ± 0.05 GPa) are reported from this area (Vielzeuf, 1980a, 1984).

2.1 The Saleix Complex

The Saleix Complex is an E-W trending, ~800 m long and ~250 m large, lens of continental basement rocks, made of granulite rocks intruded by mafic and felsic intrusives (Fig. 3). The Saleix Complex crops out in the upper part of the Saleix Valley, immediately to the east of the Saleix Pass (*Port de Saleix*), along the southern margin of the Aulus basin (Fig. 2b and 3). To the north, it is bounded by the metamorphosed Mesozoic series of the Aulus Basin, and to the south by the North Pyrenean Fault that separates it from the Carboniferous Bassies granite and the Paleozoic metasediments of the Axial Zone (Azambre & Ravier, 1978) (Fig. 2b, 2c and 3). At the Saleix Pass, an alkaline amphibole gabbro related to the Cretaceous Pyrenean magmatism crops out (Montigny *et al.*, 1986). From field relationships, it is not clear if this gabbro has intrusive relationships with the Paleozoic metasediments or if it represents a tectonic lens within the North Pyrenean Fault.

The granulitic suite is composed by three main rock types (for detailed descriptions see Azambre & Ravier, 1978; Vielzeuf, 1984; Guitard *et al.*, 1995; Ternet *et al.*, 1997): (i) leptinites and khondalite-kinzingite gneiss (aluminous, garnet-bearing acidic rocks) (Fig. 4a and b); (ii) charnockites, pyriclasites and clinopyroxenites (pyroxene-bearing acidic or basic rocks with variable proportions of Opx and Cpx) (Fig. 4c and d); and (iii) olivine/spinel-bearing marbles. Peak *P-T* conditions have been estimated within the high-pressure (HP) granulite facies at 0.8-1.0 GPa and 750-800 °C, whereas the retrograde amphibolite metamorphism equilibrated at 0.65-0.75 GPa and ~750 °C (Vielzeuf, 1979, 1980a). However, peak pressure conditions have been re-evaluated afterwards at 0.7 ± 0.05 GPa (Vielzeuf, 1984; Guitard *et al.*, 1995). The granulitic suite was intruded by basic magmas (outcropping in the eastern part of the massif; Fig. 2c and 3) that emplaced as a layered mafic complex at the base of the continental crust at ca. ~310 Ma (Vielzeuf, 1980b; Pin & Vielzeuf, 1983; Postaire, 1983; Vielzeuf & Kornprobst, 1984) (Fig. 2c and 4d to f). These magmas emplaced at granulite facies thermo-baric conditions, in a *P-T* range of 700-780 °C and 0.6-0.9 GPa (Vielzeuf, 1980b).

The Saleix Massif granulitic complex shares several lithological analogies with the well-studied Ivrea-Verbano Zone of the Southern Alps, which is widely accepted to represent a tilted section of the Adriatic pre-Alpine lower crust (Handy & Zingg, 1991; Henk *et al.*, 1997; Rutter *et al.*, 1999). There, high grade (amphibolite to granulite) metasediments (kinzingites, stronlites and marbles) are found in contact with a large (meta-) mafic complex (gabbros, diorites, norites and charnockites) (Handy & Zingg, 1991; Henk *et al.*, 1997; Rutter *et al.*, 1999; Rivalenti & Mazzucchelli, 2000; Quick *et al.*, 2009). Moreover, several mantle peridotite bodies are emplaced in the lower crustal section in the western/northwestern part of the Ivrea-Verbano Zone (e.g. Quick *et al.*, 1995 and references therein). Considering these analogies, the Saleix Massif may represent the only known example in the whole Pyrenean belt where the Variscan mafic lower crust is exposed to the surface.

After the emplacement of the layered mafic complex in the Upper Carboniferous, the Saleix granulites were further intruded by tonalitic magmas, which are not reported by previous studies (Fig. 2c and 3). This latter magmatic stage consists of amphibole-bearing felsic rocks, which intruded both the granulitic suite and the layered mafic complex, whose petrography and texture are here described for the first time.

3. Methods

A petrochronological study was carried out on representative samples of the Saleix tonalite intrusives in order to constrain their *P-T-t-d* evolution in the ductile crust. Samples were selected based on structural observations in the field (see Table 1 for sample location and constituent mineralogy). Microtextural investigations coupled with metamorphic thermobarometry were integrated to constrain the thermobaric conditions associated to the development of the shear fabrics. The chemical composition of the mineral assemblages was obtained through electron microprobe analyses (EMPA; and are presented in Supplementary Tables ST1-ST6. Zircon and titanite U-Pb geochronology was used to constrain the timing of emplacement of the tonalite intrusion(s) and the timing of the post-emplacement solid-state ductile deformation, respectively. Details on the analytical methods and protocols adopted for the U-Pb geochronology are provided in Appendix A.1.

Analytical methods and protocols adopted in this study are detailed in the Appendix. Hereafter, mineral abbreviations are after Whitney & Evans (2010).

4. Field relationships and structural data

Despite the poor outcrop conditions across the Saleix Valley, it was possible to reconstruct the intrusion/host rock relationships between the Saleix tonalite(s) and the granulitic host rocks. In the western part of the massif, the intrusive relationships between the tonalites and the granulitic host is evident (see site 2 in Fig. 3). In particular, they are emplaced in-between the garnet-bearing paragneiss (leptinites and khondalite-kinzingtonite gneiss) and the acidic and basic granulitic orthogneiss (charnockites and pyroclasticites) (Fig. 4, 5 and 6). Both the tonalitic intrusives and the granulitic host rock display a coherent ~E-W to ~ENE-WSW striking steeply dipping mylonitic foliation (Fig. 5d and 6).

In the eastern part of the massif, intrusive relationships between the tonalites and the basic charnockites (pyriclasites and anorthosites) of the layered mafic complex are less evident in the field. However, at least in one site (site 5 in Fig. 3), the tonalitic rocks have been observed in outcrop, emplaced within the layered mafic complex, even though the lateral transition with the host rocks is not fully evident. Here, magmatic foliation (when visible) is sub-vertical and strikes roughly N-S (Fig. 5a to c and 6). Evidence of a solid-state foliation is observed within cm-to-dm thick zones of ductile shear strain localization with development of S-C tectonites (cf. Gapais, 1989; Passchier & Trouw, 2005). The main attitude of the mylonitic foliation is sub-vertical with an overall ~E-W to ~ENE-WSW strike (Fig. 6). This strike is consistent with the attitude of the tectonic foliation in the mafic host rock and in the western part of the granulitic massif as described above (Fig. 5e, 5f and 6). Unfortunately, no syn-tectonic stretching lineation was observed within the deformation bands, hampering the full assessment of the shear strain from field data.

5. Texture and petrography

The tonalites dominantly display a primary igneous fabric. At the thin section scale, the tonalites show an inequigranular texture with the magmatic assemblages consisting of $Pl_1 + Amp_1 + Qz + Ep_1 + Kfs$ (with K-feldspar always < 5 vol%) and $Ttn_1 + Zrn + Ap \pm Ilm$ as accessory minerals (Table 1). The solid-state tectonic foliation is defined by the preferred orientation of recrystallized Qz ribbons, Pl_2 , $Amp_2 \pm Bt \pm Ep_2 \pm Ttn_2$ (Fig. 7; Table1). The microfabric is dominated by dynamic recrystallization of plagioclase, as attested by the ubiquitous occurrence of small recrystallized Pl_2 grains at the boundaries of larger igneous Pl_1 porphyroclasts, which typically results in core-mantle structures (Fig. 7a, b and e). Large Pl_1 grains show undulose extinction, with recrystallization being dominantly assisted by bulging and annealing, as documented by the polygonal to interlobate grain boundaries. Micro-cracking is also evident in the larger Pl_1 porphyroclasts (Fig. 7a-b, e-f). Also the amphibole shows evidence of polyphase growth, with large, strained porphyroclastic Amp_1 being often surrounded by smaller $Amp_{2,3}$ grains (Fig. 7c and d). Secondary amphibole is observed as (i) syn-tectonic metamorphic overgrowth (Amp_2) over the igneous Amp_1 (both as corona textures and in pressure shadows); and (ii) diffuse late-stage (post-tectonic) crystallization of green, fine-grained acicular-fibrous crystals (Amp_3) (Fig. 7c-f).

5.1 Titanite microfabric

Titanite is the most abundant accessory mineral and shows evidence for polyphase growth, related to the transition from magma emplacement to solid-state ductile deformation (Table 1). Three main titanite growth stages are recognized. An early generation consists of magmatic Ttn₁ grains, generally large-sized (up to 5 mm) and euhedral, with rhomboidal to rounded shapes (Fig. 7 and 8). Ttn₁ is in textural equilibrium with the magmatic assemblage and shows pre-kinematic relationships with respect to the solid-state shear foliation (Fig. 7a and e). In backscattered electron (BSE) imaging, Ttn₁ typically shows sector zoning (Fig. 8). Two subsequent generations of metamorphic titanite, Ttn₂ and Ttn₃, are recognized. Ttn₂ occurs either as: (i) recrystallized domains around Ttn₁, as attested by dark grey BSE regions truncating the original magmatic zoning (Fig. 8); and (ii) metamorphic coronas around igneous Ilm (Fig. 7c and d). Ttn₃ is fine grained (~10 µm in size) and occurs in textural equilibrium with the syn-tectonic mineral assemblage (Fig. 7c and d).

6. Mineral Chemistry

In the following, the mineral chemistry of the igneous and metamorphic assemblages of the Saleix tonalite(s) are described. Mineral compositions as obtained from EMPA and mineral formulae for primary (igneous) and secondary (metamorphic, syn- to post-tectonic) assemblages are presented in Tables ST1 to ST6 in the Supplementary Material.

Feldspar

Igneous Pl₁ shows an anorthite component (An) in the range 31-56% (average 38%, n=43; Supplementary Table ST1a). Normal compositional zoning is seldom preserved, but where evident, An-rich cores are observed ($X_{An} = 51-56\%$). Orthoclase component (Or) is always < 1%. The rare igneous Kfs (< 5 vol%) shows only a minor Na component (Ab₂₋₇Or₉₅₋₉₈) (Supplementary Table ST1a).

Secondary Pl₂ is albite (Ab)-rich and can be compositionally divided in two domains: (i) oligoclase (Pl₂) with An= 26-34% (average 30%, n=20; Supplementary Table ST1b) and (ii) albite (Pl₃) (Ab₈₀₋₉₈ An₀₁₋₁₉) (average 13%, n=7; Supplementary Table ST1c).

Amphibole

Igneous Amp₁ has SiO₂ in the range 39.55-45.84 wt%, Al₂O₃ ranging 8.06-12.54 wt% (with Al^{tot} 1.43-2.30 apfu), FeO* 16.38-24.44 wt%, CaO 11.45-12.37 wt% and TiO₂ 0.11-0.48 wt.%, corresponding to pargasite/hastingsite and Mg-hornblende (Leake *et al.* 2004; Hawthorne *et al.* 2012) compositions (Fig. 9 and Supplementary Table ST2a). The syn-tectonic Amp₂ (generally in equilibrium with Pl₂+Ep₂+Ttn₂+Bt) has SiO₂ in the range 45.75-49.57 wt%, Al₂O₃ 5.16-7.97 wt% (with Al^{tot} 0.90-1.41 apfu), FeO^{Tot} 12.54-19.60 wt%, CaO 11.25-12.65 wt% and TiO₂ 0.10-0.58 wt%, corresponding to Mg-hornblende (Leake *et al.* 2004; Hawthorne *et al.* 2012) compositions (Fig. 9 and Supplementary Table ST2b). The chemistry of the post-tectonic fibrous Amp₃ is characterized by a higher SiO₂ content (48.98-55.34 wt%), Al₂O₃ 0.81-5.46 wt% (with Al^{tot} 0.14-0.95 apfu, average value 0.60 apfu), FeO^{Tot} 7.62-18.07 wt%, CaO 11.63-12.15 wt% and TiO₂ <0.4 wt%, corresponding to tremolite (Leake *et al.* 2004; Hawthorne *et al.* 2012) compositions (Fig. 9 and Supplementary Table ST2c). In particular, considering the #Mg (atomic ratio: Mg/[Mg + Fe²⁺]) in the range 0.57–0.82 and the average Si > 7.5 apfu (Si: 7.25-7.90 apfu), the Amp₃ can be classified as actinolite (Leake *et al.* 1997; 2004).

Titanite

Primary (igneous) Ttn₁ has TiO₂ in the range 32.84-36.47 wt%, Fe₂O₃^{Tot} and Al₂O₃ ranging 0.90-2.29 wt% and 1.59-3.08 wt%, respectively (Supplementary Table ST3a). Ttn₁ shows high content of ZrO₂ (0.06-0.48 wt%), Y₂O₃ (up to 0.52 wt%), Nb₂O₅ (0.05-0.80 wt%) and ΣLREE (0.84-2.07 wt%) (Fig. 10b-c and Supplementary Table ST3a). The Ttn₂ composition has TiO₂ ranging 33.67-36.74 wt%, Fe₂O₃^{Tot} 0.70-1.72 wt%, and Al₂O₃ 1.26-2.72 wt% (Supplementary Table ST3b). Ttn₂ systematically shows lower content of ZrO₂ (0.01-0.05 wt%), Y₂O₃ (0.03-0.41 wt%), Nb₂O₅ (0.08-0.97 wt%) and ΣLREE (0.07-1.21 wt%) (Fig. 10b-c and Supplementary Table ST3c). Ttn₃ has TiO₂ in the range 33.00-38.72 wt%, Fe₂O₃^{Tot} 0.37-1.76 wt%, and Al₂O₃ 1.27-3.30 wt% (Supplementary Table ST3c). Ttn₃ shows Y₂O₃ 0.03-0.23 wt%, Nb₂O₅ 0.04-1.37 wt% and ΣLREE < 0.74 wt% (Fig. 10b-c and Supplementary Table ST3c). The ZrO₂

content is always below the detection limit of the microprobe (< 0.01 wt%). The three titanite types are therefore chemically distinct (Fig. 10), with Zr and Σ LREE contents being higher in igneous Ttn₁ and lower in metamorphic Ttn₂ and Ttn₃, respectively. Transition from igneous to metamorphic titanite growth is also characterized by the progressive enrichment in both Ti and Nb.

Epidote

Igneous (Ep₁) and metamorphic epidote (Ep₂) are chemically discriminated through their “pistacite” component ($X_{Ps}=X_{Fe}$, as atomic $[Fe^{3+}/(Fe^{3+} + Al^{3+})]$; Zen & Hammarstrom, 1984; Schmidt & Poli, 2004; Armbruster *et al.* 2006) content (Supplementary Table ST4a and ST4b, respectively). The Ep₁ is characterized by higher “pistacite” component content in the range of 22–27% (average 24%, n=25), whereas Ep₂ shows lower values (X_{Ps} : 02–21%, average 14%, n=10).

Biotite

Biotite is characterized by TiO₂ content in the range 2.26-3.11 wt% and XMg (with $XMg = [Mg/(Mg+Fe^{2+})]$ atomic ratio, calculated for 22 oxygens after Henry *et al.* 2005) in the range 0.44-0.51 (Supplementary Table ST5).

Ilmenite

Ilm is characterized by MnO 1.23-2.09 wt%, NiO < 0.08 wt% and MgO 0.11-0.34 wt% (Supplementary Table ST6).

7. Thermobarometry

In order to constrain the thermobaric conditions related to the magmatic crystallization and the solid-state deformation of the Saleix tonalite intrusives, inverse thermobarometry was applied to: (i) the primary magmatic (Pl₁ + Amp₁ + Ttn₁ + Ep₁); and (ii) the syn- (Amp₂ + Pl₂ + Ttn₂ + Ep₂ + Bt) and post- (Amp₃ + Pl₃ + Ttn₃) tectonic metamorphic assemblages.

Thermobarometry calculations were based on: (i) plagioclase-amphibole thermobarometry (Pl-Hbl; Holland & Blundy, 1994; Anderson *et al.* 2008); (ii) Al-in-hornblende barometry (Al-in-Hbl; Schmidt, 1992; Anderson *et al.* 2008); (iii) Al-in-actinolite/tremolite barometry (Al-in-Act; Schmidt, 1992; Mutch *et al.* 2016); (iv) Zr-in-titanite thermometry (Zr-in-Ttn; Hayden *et al.* 2008); and (v) Ti-in-biotite thermometry (Ti-in-Bt; Henry *et al.* 2005). The standard errors and/or approximate uncertainties reported in text are those published for Pl-Hbl, Al-in-Hbl, Al-in-Act and Ti-in-Bt models, respectively, apart from the Zr-in-Ttn model where the pooled standard error was here calculated. Results are shown in Fig. 11.

The igneous Amp₁ (Al^{tot} 1.43-2.30 apfu) and Pl₁ (for an average composition X_{An} = 38%; n=43) compositions provide $P = 0.4-0.5 \pm 0.1$ GPa (Al-in-Hbl barometry), with an average value of 0.5 ± 0.1 GPa (n=12), and $T = 670-770 \pm 30$ °C (Pl-Hbl thermometry; Holland & Blundy 1994), with an average value of $T = 700 \pm 30$ °C (n=12). The metamorphic Amp₂ (Al^{tot} 0.90-1.41 apfu) and Pl₂ (for an average composition X_{An} = 30%; n=20) compositions provide $P = 0.1-0.4 \pm 0.1$ GPa (Al-in-Hbl barometry), with an average value of 0.2 ± 0.1 GPa (n=61), and $T = 590-680 \pm 30$ °C (Pl-Hbl thermometry), with an average value of 640 ± 30 °C (n=61). The late-stage fibrous Amp₃ (Al^{tot} 0.14-0.95 apfu, average value 0.60 apfu) and Pl₃ (for an average composition of X_{An} = 13%; n=7) compositions provide $P = 0.1-0.2 \pm 0.1$ GPa (Al-in-Act barometry), with an average value of $P = 0.1 \pm 0.06$ GPa (n=65), and $T = 440-580 \pm 30$ °C (Pl-Hbl thermometry), with an average value of $T = 540 \pm 30$ °C (n=65). The obtained, Ti-independent barometric estimates are used for the Zr-in-Ttn thermometry (Hayden *et al.* 2008), (i) assuming SiO₂ activity of $a_{\text{SiO}_2}=1.0$ and TiO₂ activity of $a_{\text{TiO}_2}=0.75\pm0.25$ for rutile-free ilmenite-bearing metamorphic rocks (e.g. Hayden *et al.* 2008; Chambers & Kohn, 2012; Walters & Kohn, 2017); and (ii) converting the measured ZrO₂ (wt% \pm S.E) as derived from the EMPA into atom (Zr \pm S.E. ppm) content. To note, the EMPA measurement precision for Zr contents in Ttn₁ and Ttn₂ propagates to a further uncertainty of $\pm 2-3$ °C with respect to the calculated pooled standard error. Taking into account a lithostatic pressure of 0.5 GPa as derived from the Al-in-Hbl barometry for the magmatic Amp₁, the Zr content of Ttn₁ ($427-3550 \pm 74$ ppm) provides temperature estimates in the range $750-880 \pm 32$ °C (n=52) for the magmatic crystallization of the igneous Ttn₁. The Zr content of metamorphic Ttn₂ ($78-338 \pm 74$ ppm), for a lithostatic pressure of 0.2 GPa (Al-in-Hbl for Amp₂), provides lower temperature estimates, ranging $630-700 \pm 24$ °C (n=18). The Zr content of Ttn₃ is invariably below the detection limit of the microprobe, attesting for lower temperature conditions during the late stage, post-tectonic crystallization of the Pl₃-Amp₃-Ttn₃.

assemblage. Lastly, the Ti-in-Bt thermometry as applied to the syn-tectonic metamorphic Bt ($\text{Ti} = 0.26\text{-}0.32$ apfu and $\text{XMg} = 0.44\text{-}0.51$) provides $T = 636\text{-}688 \pm 24$ °C (with an average value of 670 ± 24 °C; $n = 19$), compatible with the mean temperature estimates obtained through $\text{Pl}_2\text{-Amp}_2$ (640 ± 30 °C) and Zr-in-Ttn₂ (667 ± 24 °C) models.

8. U-Pb geochronology

Zircon

The zircon grains from the tonalite have been investigated through BSE and cathodoluminescence imaging (Fig. 12). Their morphology varies from euhedral to subhedral, with rare anhedral crystals. They often show a dark core with oscillatory zoning and minor patchy zoning, with a homogeneous, patchy or oscillatory zoned brighter overgrowth (Fig. 12).

A number of forty-eight analyses have been performed on thirty different zircon grains. The U, Th and Pb contents and the resulting Th/U values are variable, although always greater than 0.1 (Table ST7 in the Supplementary Material). Plotted in a Tera-Wasserburg diagram (Fig. 13a), they plot, except for one analysis (S-040618a-11, Table ST7), in a concordant position within error. In particular, a first group of 19 concordant results yield a concordia date (as of Ludwig, 1998) of 281 ± 2 Ma (MSWD=0.59, Fig. 13a). These analyses were performed on the outer bright rims of the zircon crystals (Fig. 12) and yield the lowest (<0.8) Th/U values. A second group of 18 analyses performed in the core of the crystals (see Fig. 12) yield a concordia date of 300 ± 2 Ma (MSWD=0.75; Fig. 13a), with the highest (>0.8) Th/U values. Finally, the remaining results (dotted-line grey ellipses on Fig. 13a) plot either around the two previously described date groups or yield apparent ages of ca. 450 Ma and 550 Ma, respectively. These last four data have been systematically obtained in zircon crystal cores (see for example Zr 12 and Zr 28 on Fig. 12).

Titanite

Forty-one analyses have been acquired on the large magmatic Ttn₁ grains (Table ST8). They all plot in a very discordant position in the Tera-Wasserburg diagram (Fig. 13c). Unfortunately, these data do not allow to calculate any date. Significantly, however, all the data plot in a crisis polygon as defined by a common Pb composition $(^{207}\text{Pb}/^{206}\text{Pb})_0 = \text{ca } 0.85$ (calculated using the Stacey & Kramers (1975) Pb evolution model for an age of ca. 300 Ma), the date yielded by the outer rims of the zircon grains (ca. 281 Ma) and the date yielded by the metamorphic Ttn₂ grains (ca. 96 Ma; see below).

Forty analyses have been performed in the metamorphic Ttn₂ grains, overgrowing Ilm (Fig. 13b and Table ST8 in the Supplementary Material). The U, Th and Pb contents (3-23, 1-12 and 7-43 ppm respectively) and the Th/U values (0.3-2.0) are fairly consistent for all the analyses. Plotted in a Tera-Wasserburg diagram (Fig. 13b), they all plot in a discordant position with variable proportion of common Pb. The 40 analyses, however, define a lower intercept date of 96.5 ± 2.1 Ma (MSWD=2.1) and a $(^{207}\text{Pb}/^{206}\text{Pb})_0$ value of 0.86 ± 0.01 .

9. Discussion

Field relationships indicate that the tonalitic magmas intruded the Saleix granulitic and the layered mafic complex. Moreover, textural and petrographic observations show that a solid-state syn-tectonic metamorphic event locally overprinted the primary magmatic texture.

Considering an average lithostatic gradient of 0.028 GPa/km, the *P-T* conditions of emplacement of the Saleix tonalite as derived from the Al-in-Hbl barometry (on Amp₁) and Zr-in-Ttn₁ thermometry ($P = 0.5 \pm 0.1$ GPa and $T = 750\text{-}880 \pm 32$ °C) are indicative of intermediate crustal depths (~18 km) and paleogeothermal gradient conditions higher than 45 °C/km. These emplacement depths are significantly shallower than those estimated both for the peak metamorphism of the granulitic suite (25 ± 1.8 km; Vielzeuf, 1984) and for the emplacement of the layered mafic complex (ca. 23-33 km; Vielzeuf, 1980b) forming the host rocks.

Taking into account the results of the conventional thermobarometry applied to the different generations of the syn-tectonic mineral assemblage (Amp₂₋₃, Pl₂₋₃, Ttn₂₋₃), the solid-state ductile deformation occurred under amphibolite facies metamorphic conditions (0.2 ± 0.1 GPa and $640\text{--}670 \pm 30$ °C). The observed plagioclase recrystallization microstructures (mainly bulging) are indicative of medium-grade conditions (i.e. 400–600 °C) during solid-state ductile deformation (e.g. Gapais, 1989; Tullis & Yund, 1991; Rosenberg & Stünitz, 2003; Passchier & Trouw, 2005), consistent with the temperature estimates as derived from the mineral-chemistry thermometry models applied to the syn-tectonic metamorphic assemblage. Assuming the same average lithostatic gradient of 0.028 GPa/km, the syn-tectonic, solid-state amphibolite-facies metamorphic overprint took place at shallow crustal conditions (less than ~10 km depth), corresponding to a perturbed geothermal gradient of ca. 80 °C/km.

The presence of datable mineral phases associated with both the magmatic and the metamorphic syn-tectonic mineral assemblages allows to chronologically constrain the *P-T-d* history of the Saleix tonalite. The zircon U-Pb geochronology documents a bimodal age distribution. Most of the zircon core dates cluster at ca. 300 Ma (late Carboniferous; Fig. 12 and 13a), which is in good agreement with the emplacement age of the layered mafic complex intruded by the tonalite (Pin & Vielzeuf, 1983; Postaire, 1983; Vielzeuf & Kornprobst, 1984; Pin, 1989). Zircon rim dates and most of the rim/core coherent dates cluster around 281 Ma (Early Permian; Fig. 12 and 13a), which is then interpreted as the crystallization age of the tonalitic intrusion. This interpretation is further supported by the Th/U values in zircon (always > 0.1; Table ST7), which are consistent with a magmatic origin (see Rubatto 2002; Kydonakis et al. 2014 and references therein). These results suggest a recycling of zircon grains of the mafic host-rocks in the crystallising tonalite. This interpretation is consistent with other studies on xenocrystic zircon entrainment in plutons and dikes (e.g. Viskupic *et al.* 2005). Another possibility would be that the tonalite was emplaced at ca. 300 Ma and that all the younger dates around 280 Ma are linked to a slight Pb loss in the analysed zircon grains. But because of the intrusive relationship between the tonalites and the mafic complex, this scenario seems unlikely. Whatever the scenario, the oldest apparent ages of 550 and 450 Ma are interpreted as the ages of inherited (xenocrystic) cores. We thus infer that the tonalitic magma could have been contaminated by zircon crystals not only from the mafic complex but also from the para-derived granulitic host-rock.

Activation of solid-state syn-tectonic fabric is constrained by the U-Pb dating of Ttn₂. The lower intercept of the Ttn₂ discordia with the concordia curve at 96 ± 2 Ma (Cenomanian; Fig. 13b) defines the minimum age for the tectonic overprint of the Pyrenean Variscan lower crust. This Cenomanian age is well compatible with the mid-Cretaceous Pyrenean rifting event that led to the final exhumation of the lithospheric mantle in the Pyrenean realm (e.g. Lagabrielle *et al.* 2010). The disturbed signal displayed by the magmatic Ttn₁ (Fig. 13c) is likely due to the incomplete re-opening of the titanite U-Pb system during the activation of the Cretaceous ductile deformation fabric, leading to variable amount of Pb loss (see Garber *et al.* 2017). However, it is important to note that the diffusion rate of Pb in titanite is quite low at $T < 750$ °C (see Kohn 2017; Holder *et al.* 2019), and it is likely that some recrystallization, rather than diffusion alone, occurred in these domains. The size of the laser ablation spot used in this study (35 µm) for the U-Pb dating on Ttn was indeed too large compared to the size of the preserved/recrystallized domains to properly discriminate the magmatic event from the metamorphic one in the disturbed magmatic Ttn₁.

9.1 Permian thinning of the Pyrenean crust

The timing of exhumation of the lower granulitic crust in the Pyrenees and the modes through which the lower crust accommodated deformation during the Cretaceous rifting have been a matter of debate during the last decade (e.g. Jammes *et al.* 2009; Clerc & Lagabrielle, 2014; Masini *et al.* 2014; Hart *et al.*, 2016; Asti *et al.* 2019; Duretz *et al.* 2019; Espurt *et al.* 2019; Saspiturry *et al.* 2019; Odlum & Stockli, 2020). Some authors have proposed that lower crustal granulites have been exhumed during the Albian-Cenomanian by low-angle detachment faulting in the Labourd massif (western Pyrenees; Jammes *et al.* 2009; Masini *et al.* 2014). However, this interpretation has been questioned by recent studies documenting the Permian exhumation of the granulitic/migmatitic Ursuya massif at the footwall of the south-dipping Louhossoa shear zone, in relationship with the formation of the Permo-Triassic Bidarray basin in the hanging wall (Saspiturry *et al.* 2019).

Although several studies have pointed out a significant Permian episode of crustal stretching and thinning in the Pyrenean realm (e.g. de Saint Blanquat *et al.* 1990; Bouhallier *et al.* 1991; Vissers, 1992; de Saint Blanquat, 1993; Boutin *et al.* 2016; Saspiturry *et al.*

2019), these studies did not provide proper constraints on the evolution of the post-Variscan crustal structure. A recent cross-section restoration across the central part of the Pyrenean belt (Aure valley) suggests a thinning of the continental crust down to ~20 km as a consequence of the Permian rifting phase (Espurt *et al.* 2019).

Considering the intrusive/host-rock relationships in the Saleix Complex, the pressure gap between the emplacement of the layered mafic complex at ca. 300 Ma (at 0.6-0.9 GPa; Vielzeuf, 1980b) and intrusion of the tonalitic magmas at ca. 280 Ma (at ~0.5 GPa) provides evidence for a significant phase of exhumation of the lower part of the crust at the Carboniferous-Permian transition. This in turn requires that a considerable thinning of the north Pyrenean continental crust took place during the Early Permian, with the lower part of the crust (represented by the Saleix Complex) exhumed from ~25-30 km to ~18 km depths within this time frame (Fig. 14a, b). This extensional phase is coeval with partial melting of the lower-middle crust and emplacement of gneiss domes in the middle-upper crust in the Pyrenean Axial Zone (e.g. Delène *et al.* 2012; Cochelin *et al.* 2017; Lemirre *et al.*, 2019), and with low-P granulitic metamorphism and subsequent crustal extension in the North Pyrenean Massifs (de Saint Blanquat *et al.* 1990; de Saint Blanquat, 1993; Fig. 14a). In these massifs, the Permian extensional phase has been assumed to have caused up to ~10 km of thinning of the Variscan crust (Bouhallier *et al.* 1991), accommodating an overall N-S oriented, top to the S stretching (de Saint Blanquat *et al.* 1990; Bouhallier *et al.* 1991; de Saint Blanquat, 1993). This is consistent with estimates of at least 10 km of exhumation during the same time frame in the Pyrenean Axial Zone, even though driven by a general E-W direction of stretching (Vissers, 1992; Cochelin *et al.*, 2017; Lemirre *et al.*, 2019). Additional evidence for a significant late-/post-Variscan thinning comes from petrographic studies on the continental mantle section(s) exhumed along the Pyrenean belt, which highlighted an important phase of lithospheric thinning before the Triassic (Fabriès *et al.* 1991, 1998), likely in relationship with the Permian re-fertilization of the lithospheric mantle (Le Roux *et al.* 2007). Moreover, as mentioned above, this is also consistent with estimates of pre-Triassic thinning of the Pyrenean continental crust down to ~20 km of total thickness based on a balanced cross-section across the Central Pyrenees (Espurt *et al.* 2019).

Our estimates of paleogeothermal gradient at the time of intrusion of the Saleix tonalite intrusives (> 45 °C/km) are coherent with other estimates of the (late?) Variscan geothermal gradients reported by previous studies in the Pyrenean realm (40-70 °C/km; Gibson &

Bickle, 1994; Mezger, 2005; Triboulet *et al.* 2005; Vilà *et al.* 2007; Mezger & Régnier 2016; Cochelin *et al.* 2018). This reinforces our interpretation of the thermobaric conditions of emplacement of the Saleix tonalite during the Early Permian.

From a geodynamic point of view, the late-/post-Variscan Permian extensional phase can be related to the (late- ?) post-orogenic dismantling of the Variscan belt (e.g. Malavieille *et al.* 1990; Van Den Driessche & Brun, 1992; Burg *et al.* 1994), which is coeval with lithospheric mantle delamination at the scale of the western European portion of the belt (Ziegler *et al.* 2004, 2006; Ziegler & Dèzes, 2006; Laurent *et al.*, 2018), including the Pyrenean realm (e.g. Denèle *et al.* 2014; Cochelin *et al.* 2017). This resulted in a substantial thinning of the whole Pyrenean continental lithosphere (e.g. Fabriès *et al.* 1991, 1998), which isostatically allowed the subsistence of a continental sedimentary setting at the Iberia/Eurasia plate boundary (and in western Europe in general) during the Permian.

9.2 Implications for the Cretaceous rifting

As constrained by the syn-tectonic growth of metamorphic Ttn₂ (dated at 96 ± 2 Ma), the solid-state deformation fabric documented in the Saleix Complex occurred during the regional-scale mid-Cretaceous rifting event (Fig. 14c). At this stage, the Pyrenean continental crust was already extremely thinned, with the lower part of the Variscan crust having been already exhumed at shallow depths (≤ 0.2 GPa; see Section 7). Consequently, at the onset of the Cretaceous rifting, the thickness of the Variscan crust might have been the cumulative result of multiple rifting events throughout the Mesozoic. Indeed, between the Lower Permian extensional phase and the Cretaceous rifting, it is likely that the crust was progressively and incrementally thinned during the several aborted rifting episodes that affected the Pyrenean realm between the Upper Permian/Triassic and the Aptian (e.g. Puigdefabregas & Souquet, 1986; Barnolas & Chiron, 1995; Vergés & García-Senz, 2001; Vergés *et al.* 2002; Espurt *et al.* 2019). Additional evidence for a pre-Cretaceous thinning of the Pyrenean crust comes from the *P-T-t-d* evolution of the exhumed lithospheric mantle outcropping in the North Pyrenean Zone. Indeed, the Cretaceous extensional mylonitic shear zone of the Turon de la Técoùère ultramafic massif (western Pyrenees) developed at relatively shallow depths, at pressures as low as ~ 0.5 GPa (Fabriès *et al.* 1998; Newman *et al.* 1999).

During the Cretaceous rifting, the Pyrenean realm experienced a well known thermal event, documented by the high temperature/low pressure (HT/LP) metamorphism on the Mesozoic pre- and syn-rift series (Albarède & Michard-Vitrac, 1978; Montigny *et al.* 1986; Golberg, 1987; Golberg & Maluski, 1988; Golberg & Leyreloup, 1990; Clerc *et al.* 2015). In this regard, our paleogeothermal estimates of > 80 °C/km is in agreement with other estimates dealing with the Cretaceous Pyrenean rifting (e.g. Vacherat *et al.* 2014; Corre, 2017; Hart *et al.* 2017; Saspiturry *et al.*, 2020), supporting our interpretation of the *P-T-t-d* history of the Saleix Complex.

Several studies in the last decade have inferred that ductile deformation localized in the exhumed lower granulitic crust during the Cretaceous mantle exhumation, and not only in the middle/upper part of the crust (e.g. Clerc & Lagabriele, 2014; Asti *et al.* 2019; Duretz *et al.* 2019). The Cretaceous ductile deformation described in this study fits well in this scenario. In this regard, our dataset demonstrates that during the Cretaceous Pyrenean rifting the deformation of the lower part of the continental crust was assisted by ductile flow. This evidence is in contrast with models of crustal thinning proposed for other types of rifted margins, where the lower granulitic crust is considered to be dominated by brittle deformation mechanisms and ductile flow mechanisms are assumed to be localised in the middle crust, which represents a decoupling horizon between the brittle upper and lower crust (e.g. Péron-Pinvidic & Manatschal, 2009; Mohn *et al.*, 2012). The peculiar rheological behaviour of the Pyrenean crust during the Cretaceous rifting has been recently referred to the pre-rift mechanical configuration of the crust, which is characterized by the presence of a thick weak decoupling layer at the base of the sedimentary cover consisting in the Keuper evaporitic series (e.g. Lagabriele *et al.*, 2020; Saspiturry *et al.*, 2021). This pre-rift crustal structure allowed the ductile deformation to localize at all levels in the continental crust during the Cretaceous rifting (Duretz *et al.* 2019).

Conclusion

The petrochronological study presented in this paper allows to reconstruct the long-term *P-T-t-d* history of the Saleix tonalites and of its granulitic host rocks, with important inferences on the long-term evolution of the post-Variscan Pyrenean continental crust. The main conclusions of this work can be summarized as follows:

- The emplacement of the Saleix tonalite in the Variscan crust occurred at 281 ± 2 Ma (Early Permian), ca. 20-30 Myr after mafic magma underplating at the base of the granulitic crust.
- The pressure gap between the emplacement of the Saleix tonalite (ca. 0.5 GPa) and its lower crustal host rock (0.6-0.9 GPa) provides evidence for a significant thinning of the Pyrenean crust (~20 km of total thickness) between the end of the Carboniferous and the Early Permian.
- Solid-state ductile deformation is documented in the Variscan lower crust during the mid-Cretaceous rifting event that culminated with lithospheric mantle exhumation.
- At the onset of the Cretaceous rifting, the Pyrenean continental crust was already extremely thinned by rifting events that localized in this domain since the end of the Variscan cycle.

More generally, this study confirms the importance of structural inheritance (in space and time) during the deformation of the continental crust. As a matter of fact, the peculiar evolution of the Pyrenean crust and lithosphere was possibly due to its position in the Carboniferous foreland basin of the Hercynian orogen of western Europe, a domain that experienced a peculiar syn-, late- and post-Variscan evolution. This complex evolution was characterized by limited syn-orogenic thickening, but important late-/post-orogenic crustal thinning and mantle delamination. Inheritance of these events had a strong impact on the Mesozoic and Cenozoic evolution of a region that accommodated the deformation at the boundary between the Iberian and Eurasian plates over a very long period of time.

Declaration of interests

The authors declare that they have no known competing financial interests or personal relationships that could have appeared to influence the work reported in this paper.

Acknowledgments

This work has been carried on in the frame of the Orogen Project (BRGM + Total + CNRS-INSU; <https://convergent-margins.com/orogen/>) which provided a post-doc grant to R. A. The manuscript benefitted from insightful comments and reviews by Zheng-Xiang Li (Editor), Bruno Ribeiro and Jesse Walters. We thank Thomas Theye for his precious suggestions and for reviewing an early version of this manuscript. Jessica Langlade is thanked for her kind assistance during EMPA analyses at the Service Commun de Microsonde Ouest (SCMO), Plouzané (France). We also thank Serge Fourcade for fruitful discussions and for sharing his knowledge on the study area. Nicolas Saspiturry is thanked for its assistance and stimulating discussions in the field. Yann Lepagnot provided mineral separates for zircon dating. We acknowledge the GeOHeLiS platform for the cathodoluminescence and LA-ICP-MS facilities.

R. A. wish to express his eternal gratitude to Jean-Pierre Brun for introducing him to the fascinating world of plate tectonics. This paper is humbly dedicated to his memory.

Credit Author Statement of the article:

Polyphase post-Variscan thinning of the North Pyrenean crust: Constraints from the P-T-t-deformation history of the exhumed Variscan lower crust (Saleix Massif, France)

by

Riccardo Asti, Federico Rossetti, Federico Lucci, Marc Poujol, Yves Lagabrielle

Riccardo Asti: Conceptualization, Validation, Investigation, Writing - Original Draft, Visualization, Supervision, Project administration;

Federico Rossetti: Conceptualization, Formal analysis, Investigation, Writing - Review & Editing, Visualization; **Federico Lucci:**

Formal analysis, Investigation, Data Curation, Writing - Review & Editing, Visualization; **Marc Poujol:** Formal analysis, Investigation,

Resources, Data Curation, Writing - Review & Editing, Visualization; **Yves Lagabriele**: Writing - Review & Editing, Funding acquisition.

Appendix A. Analytical methods and protocols

A.1. U-Pb geochronology

After the rock sample was crushed, zircon grains were concentrated using a Wifley table then the heavy liquors and magnetic techniques available at Géosciences Rennes (France). The zircon grains were randomly selected to be mounted in epoxy mounts, and then polished in order to obtain a smooth flat internal surface. In order to inspect the internal structure and choose the potential internal target sites for the U-Pb laser ablation-inductively coupled plasma-mass spectrometry (LA-ICP-MS) dating, cathodoluminescence imagery were acquired.

For the titanite dating, the in-situ LA-ICP-MS analyses were performed in-context, directly in thin sections.

The U-Pb geochronology was conducted at using an ESI NWR193UC Excimer laser coupled to a quadripole Agilent 7700x ICP-MS, a GeOHeLiS platform facility. The instrumental conditions are reported in Supplementary Table ST9. The ablated material is carried into helium, and then mixed with nitrogen and argon, before injection into the plasma source. The alignment of the instrument and mass calibration was performed before each analytical session using the NIST SRM 612 reference glass, by inspecting the ^{238}U signal and by minimizing the ThO^+/Th^+ ratio ($<0.5\%$). During the course of an analysis, the signals of $^{204}(\text{Pb}+\text{Hg})$, ^{206}Pb , ^{207}Pb , ^{208}Pb , ^{232}Th and ^{238}U masses are acquired. The occurrence of common Pb in the sample can be monitored by the evolution of the $^{204}(\text{Pb}+\text{Hg})$ signal intensity, but no common Pb correction was applied owing to the large isobaric interference with Hg. Single analyses consisted of 20 s of background integration followed by 60 s integration with the laser firing. Ablation spot diameters of 25 μm (zircon) and 35 μm (titanite) with repetition rates of 4 Hz and a fluence of $6.8\text{J}/\text{cm}^2$ were used. Data were corrected for U-Pb and Th-Pb fractionation and

for the mass bias by standard bracketing with repeated measurements of the zircon reference material GJ-1 (for zircon dating; Jackson *et al.* 2004) and titanite reference material Khan (for titanite dating; Heaman, 2009). Along with the unknowns, zircon standard Plešovice (337 Ma, Sláma *et al.* 2008) and titanite standard LAC (520 Ma, Pedersen *et al.* 1989) were measured to monitor precision and accuracy of the analyses and yield precise with low bias ages of 336.4 ± 3.6 Ma and 512 ± 9 Ma respectively (Table ST9 in Supplementary Material). Data reduction was performed using *Iolite* (Paton *et al.* 2010; 2011) with the *VizualAge* U–Pb data reduction package for zircon (Petrus & Kamber, 2012) and *VizualAge_UcomPbine* for titanite (Chew *et al.* 2014). For data processing, we used a $^{235}\text{U}/^{238}\text{U}$ ratio of 137.818 (Hiess *et al.* 2012). All the concordia diagrams and age calculations (Fig. 13) were produced using *IsoplotR* (Vermeesch, 2018). All errors are provided at 2 sigma.

A.2. Electron microprobe analysis (EMPA)

The major elements composition of the main mineral components was determined by EMPA, by using a CAMECA SX100 microprobe at the Service Commun de Microsonde Ouest (SCMO), Plouzané (France). Microprobe operated at 15 kV, 20nA, spot size 5 μm and 10 s counting time on peak and 5 s on background. The microprobe was equipped with five WDS detectors with LIF, PET, and TAP crystals, and all elements were assigned to specific detectors to be measured 5 + 5 concurrently per run of ~30 s total time. Used standards were natural albite (Na, Si), orthoclase (K), corundum (Al), wollastonite (Ca), forsterite (Mg), MnTiO_3 (Mn, Ti), andradite (Fe) and chromite (Cr). Raw spectral data were ZAF-corrected using the phi-rho-Z protocol of Pouchou & Pichoir (1984) known as ‘PAP’. Element contents were recalculated to oxides by stoichiometry, total iron content is represented as FeO. Detection limits are: 0.01 wt% for Mn, Ti, Fe, Ni and Cr; 0.05 wt% for Ca, Si and K; 0.10 wt% for Al, Mg and Na.

The chemical composition of Ttn was measured by a Cameca SX100 microprobe at the Institut für Anorganische Chemie, Universität Stuttgart, Germany. The REE La, Ce, Pr, Nd, and Sm were measured applying LIF/LLif diffraction crystals, using synthetic orthophosphates (Jarosewich & Boatnar 1991; Donovan *et al.* 2003) as standards. Additional elements were analysed with the following standards: synthetic BaF₂ (F), synthetic corundum (Al; P&H Developments), natural wollastonite (Si, Ca; P&H

Developments, England), natural graftedite (P), synthetic rutile (Ti; P&H Developments), natural rhodonite (Mn; P&H Developments), natural hematite (Fe; P&H Developments), synthetic YPO₄ (Y; Jarosewich & Boatnar 1991), and synthetic Nb (P&H Developments). Operating conditions of the microprobe were 15 or 20 kV, 100 nA, 5 µm spot size. With these conditions, REE, Zr, Y and Nb have detection limits as based on counting statistics and 1sigma uncertainties in the range of 0.01 to 0.03 wt.%, 0.01 wt%, 0.02 wt% and 0.02 wt% of the elements, respectively.

Feldspar, epidote, biotite and ilmenite structural formulae were calculated using the Calcmin_32 Excel spreadsheet (Brandelik, 2009). Amphibole formulae (normalization scheme: 15-NK) were calculated through the ACES2013 Excel spreadsheet (Locock, 2014). Mineral abbreviations follow Whitney & Evans (2010).

Supplementary data

Supplementary material 1

Supplementary material 2

Supplementary material 3

Supplementary material 4

References

- Albarède, F. & Michard-Vitrac, A. 1978. Age and significance of the North Pyrenean metamorphism. *Earth and Planetary Science Letters*, **40**, 327–332, [https://doi.org/10.1016/0012-821X\(78\)90157-7](https://doi.org/10.1016/0012-821X(78)90157-7).
- Anderson, J.L. Barth, A.P. Wooden, J.L. & Mazdab, F. 2008. Thermometers and thermobarometers in granitic systems. *Reviews in Mineralogy and Geochemistry*, **69**, 121–142, <https://doi.org/10.2138/rmg.2008.69.4>.

- Andrieux, P. 1982. Conditions de cristallisation et évolution paragénétique d'une charnockite hercynienne: le complexe granulitique d'Ansignan (massif de l'Agly, Pyrénées orientales). *Bulletin Minéralogique*, **105**, 253-266.
- Armbruster, T. Bonazzi, P. Akasaka, M. Bermanec, V. Chopin, C. Gieré, R. ... Pasero, M. 2006. Recommended nomenclature of epidote-group minerals. *European Journal of Mineralogy*, **18**(5), 551–567, doi:10.1127/0935-1221/2006/0018-0551
- Asti, R. Lagabriele, Y. Fourcade, S. Corre, B. & Monié, P. 2019. How Do Continents Deform During Mantle Exhumation? Insights From the Northern Iberia Inverted Paleopassive Margin, Western Pyrenees (France). *Tectonics*, **38**, 1666–1693, <https://doi.org/10.1029/2018TC005428>.
- Autran, A. Carreras, J. Durand-Delga, M. & Laumonier, B. 1995. Le cycle hercynien dans les Pyrénées. Réflexions géodynamiques finales. In Barnolas, A. & Chiron, J.C. eds. *Synthèse géologique et géophysique des Pyrénées*. Édition BRGM - ITGE, vol. **1**.
- Azambre, B. & Guitard, G. 2001. Disthène et staurotide reliques dans les métapelites du Canigou (Pyrénées orientales). Relations avec les épisodes hercyniens de basse et moyenne pressions. *Comptes Rendus de l'Académie de Sciences - Serie IIa: Sciences de la Terre et des Planètes*, **333**, 601–609, [https://doi.org/10.1016/S1251-8050\(01\)01670-6](https://doi.org/10.1016/S1251-8050(01)01670-6).
- Azambre, B. & Ravier, J. 1978. Les ecailles de gneiss du facies granulite du Port de Saleix et de la région de Lherz (Ariege), nouveaux témoins du socle profond des Pyrénées. *Bulletin de la Société Géologique de France*, **S7-XX**, 221–228, <https://doi.org/10.2113/gssgfbull.s7-xx.3.221>.
- Barnolas, A. & Chiron, J.C. 1995. Synthèse géologique et géophysique des Pyrénées - Volume 2: Cycle alpin: Stratigraphie. Édition BRGM - ITGE.
- Bixel, F. & Lucas, C. L. 1983. Magmatisme, tectonique et sédimentation dans les fossés stéphano-permiens des Pyrénées occidentales. *Revue de géologie dynamique et de géographie physique*, **24** (4), 329–342.
- Bouhallier, H. Choukroune, P. & Ballevre, M. 1991. Evolution structurale de la croûte profonde Hercynienne: exemple du massif de l'Agly (Pyrénées Orientales, France). *Comptes Rendus - Académie des Sciences, Serie II*, **312**, 647–654.
- Boutin, A. de Saint Blanquat, M. Poujol, M. Boulvais, P. de Parseval, P. Rouleau, C. & Robert, J.F. 2016. Succession of Permian and Mesozoic metasomatic events in the eastern Pyrenees with emphasis on the Trimouns talc–chlorite deposit. *International Journal of Earth Sciences*, **105**, 747–770, <https://doi.org/10.1007/s00531-015-1223-x>.
- Brandelik, A. 2009. CALCMIN - an EXCEL™ Visual Basic application for calculating mineral structural formulae from electron microprobe analyses. *Computers and Geosciences*, **35**, 1540–1551, <https://doi.org/10.1016/j.cageo.2008.09.011>.
- Burg, J.P. Van Den Driessche, J. & Brun, J.P. 1994. Syn- to post-thickening extension in the Variscan Belt of Western Europe: modes and structural consequences. *Geologie de la France*, **3**, 33–51.

- Chambers, J.A. & Kohn, M.J. 2012. Titanium in muscovite, biotite, and hornblende: Modeling, thermometry, and rutile activities of metapelites and amphibolites. *American Mineralogist*, **97**(4), 543–555, doi:10.2138/am.2012.3890
- Chew, D.M. Petrus, J.A. & Kamber, B.S. 2014. U-Pb LA-ICPMS dating using accessory mineral standards with variable common Pb. *Chemical Geology*, **363**, 185–199, <https://doi.org/10.1016/j.chemgeo.2013.11.006>.
- Choukroune, P. 1976. Structure et évolution tectonique de la zone Nord-pyrénéenne. Analyse de la déformation dans une portion de chaîne à schistosité sub-verticale. *Mem Soc géol France*, **55**, 1–116.
- Choukroune, P. & Mattauer, M. 1978. Tectonique des plaques et Pyrenées; sur le fonctionnement de la faille transformante nord-pyrénéenne; comparaisons avec des modèles actuels. *Bulletin de la Société Géologique de France*, **S7-XX**, 689–700, <https://doi.org/10.2113/gssgfbull.s7-xx.5.689>.
- Clerc, C. & Lagabrielle, Y. 2014. Thermal control on the modes of crustal thinning leading to mantle exhumation: Insights from the Cretaceous Pyrenean hot paleomargins. *Tectonics*, **33**, 1340–1359, <https://doi.org/10.1002/2013TC003471>.
- Clerc, C. Lahfid, A. *et al.* 2015. High-temperature metamorphism during extreme thinning of the continental crust: A reappraisal of the North Pyrenean passive paleomargin. *Solid Earth*, **6**, 643–668, <https://doi.org/10.5194/se-6-643-2015>.
- Cochelin, B. Chardon, D. Denèle, Y. Gumiaux, C. & Le Bayon, B. 2017. Vertical strain partitioning in hot Variscan crust: Syn-convergence escape of the Pyrenees in the Iberian-Armorican syntax. *Bulletin de la Société Géologique de France*, **188**, <https://doi.org/10.1051/bsgf/2017206>.
- Cochelin, B. Lemirre, B. Denèle, Y. Blanquat, M. de S. Lahfid, A. Duchêne, S. 2018. Structural inheritance in the Central Pyrenees: the Variscan to Alpine tectonometamorphic evolution of the Axial Zone. *Journal of the Geological Society*, **175**, 336–351. <https://doi.org/10.1144/jgs2017-066>
- Corre, B. 2017. La bordure nord de la plaque ibérique à l'Albo-Cénomane. Architecture d'une marge passive de type ductile (Chaînon Béarnais, Pyrénées Occidentales). *PhD thesis*, 320 pp. Université de Rennes 1, France.
- Corre, B. Lagabrielle, Y. Labaume, P. Fourcade, S. Clerc, C. & Ballèvre, M. 2016. Deformation associated with mantle exhumation in a distal, hot passive margin environment: New constraints from the Sarailh Massif (Chaînon Béarnais, North-Pyrenean Zone). *Comptes Rendus - Geoscience*, **348**, 279–289, <https://doi.org/10.1016/j.crte.2015.11.007>.
- Corre, B. Boulvais, P. Boiron, M.C. Lagabrielle, Y. Marasi, L. & Clerc, C. 2018. Fluid circulations in response to mantle exhumation at the passive margin setting in the north Pyrenean zone, France. *Mineralogy and Petrology*, **112**, 647–670, <https://doi.org/10.1007/s00710-018-0559-x>.
- de Hoym de Marien, L. Le Bayon, B. Pitra, P. Van Den Driessche, J. Poujol, M. & Cagnard, F. 2019. Two-stage Variscan

- metamorphism in the Canigou massif: Evidence for crustal thickening in the Pyrenees. *Journal of Metamorphic Geology*, **37**, 863–888, <https://doi.org/10.1111/jmg.12487>.
- de Saint Blanquat, M. Lardeaux, J.M. & Brunel, M. 1990. Petrological arguments for high-temperature extensional deformation in the Pyrenean Variscan crust (Saint Barthélémy Massif, Ariège, France). *Tectonophysics*, **177**, 245–262, [https://doi.org/10.1016/0040-1951\(90\)90284-F](https://doi.org/10.1016/0040-1951(90)90284-F).
- de Saint Blanquat, M. Bajolet, F. *et al.* 2016. Cretaceous mantle exhumation in the central Pyrenees: New constraints from the peridotites in eastern Ariège (North Pyrenean zone, France). *Comptes Rendus - Geoscience*, **348**, 268–278, <https://doi.org/10.1016/j.crte.2015.12.003>.
- de Saint Blanquat, M. 1993. La faille normale ductile du massif du Saint Barthelemy. Evolution hercynienne des massifs nord-pyreneens catazonaux considerée du point de vue de leur histoire thermique. *Geodinamica Acta*, **6**, 59–77, <https://doi.org/10.1080/09853111.1993.11105239>.
- Debroas, E.J. 1987. Modèle de bassin triangulaire à l'intersection de décrochements divergents pour le fossé albo-cénomanién de la Ballongue (zone nord-pyrénéenne, France). *Bulletin de la Société Géologique de France*, **8**, 887–898, <https://doi.org/10.2113/gssgfbull.III.5.887>.
- Debroas, E.J. 1990. Le Flysch noir albo-cenomanien témoin de la structuration albienne à senonienne de la Zone nord-pyrénéenne en Bigorre (Hautes-Pyrénées, France). *Bulletin - Société Géologique de France*, **6**, 273–285, <https://doi.org/10.2113/gssgfbull.vi.2.273>.
- Delaperrière, E. de Saint Blanquat, M. Brunel, M. & Lancelot, J. 1994. Géochronologie U-Pb sur zircons et monazites dans le Massif du Saint Barthélémy (Pyrénées, France): Discussion des âges des événements varisques et pré-varisques. *Bull. Soc. Géol de France*, **165**, n°2, 101–112.
- Denèle, Y. Paquette, J.L. Olivier, P. & Barbey, P. 2012. Permian granites in the Pyrenees: The Aya pluton (Basque Country). *Terra Nova*, **24**, 105–113, <https://doi.org/10.1111/j.1365-3121.2011.01043.x>.
- Denèle, Y. Laumonier, B. Paquette, J.L. Olivier, P. Gleizes, G. & Barbey, P. 2014. Timing of granite emplacement, crustal flow and gneiss dome formation in the Variscan segment of the Pyrenees. *Geological Society Special Publication*, **405**, 265–287, <https://doi.org/10.1144/SP405.5>.
- Donovan, J.J. Hanchar, J.M. Picolli, P.M. Schrier, M.D. Boatner, L.A. & Jarosewich, E. 2003. A re-examination of the rare-earth-element orthophosphate standards in use for electron-microprobe analysis. *Canadian Mineralogist*, **41**, 221–232, <https://doi.org/10.2113/gscanmin.41.1.221>.
- Duretz, T. Asti, R. Lagabriele, Y. Brun, J.P. Jourdon, A. Clerc, C. & Corre, B. 2019. Numerical modelling of Cretaceous Pyrenean

- Rifting: The interaction between mantle exhumation and syn-rift salt tectonics. *Basin Research*, 1–16, <https://doi.org/10.1111/bre.12389>.
- Espurt, N. Angrand, P. Teixell, A. Labaume, P. Ford, M. de Saint Blanquat, M. & Chevrot, S. 2019. Crustal-scale balanced cross-section and restorations of the Central Pyrenean belt (Nestes-Cinca transect): Highlighting the structural control of Variscan belt and Permian-Mesozoic rift systems on mountain building. *Tectonophysics*, **764**, 25–45, <https://doi.org/10.1016/j.tecto.2019.04.026>.
- Fabries, J. Lorand, J.P. Bodinier, J.L. & Dupuy, C. 1991. Evolution of the upper mantle beneath the pyrenees: Evidence from orogenic spinel lherzolite massifs. *Journal of Petrology*, **Special-Vo**, 55–76, https://doi.org/10.1093/petrology/Special_Volume.2.55.
- Fabriès, J. Lorand, J.P. & Bodinier, J.L. 1998. Petrogenetic evolution of orogenic lherzolite massifs in the central and western Pyrenees. *Tectonophysics*, **292**, 145–167, [https://doi.org/10.1016/S0040-1951\(98\)00055-9](https://doi.org/10.1016/S0040-1951(98)00055-9).
- Ford, M. Hemmer, L. Vacherat, A. Gallagher, K. & Christophoul, F. 2016. Retro-wedge foreland basin evolution along the ECORS line, eastern Pyrenees, France. *Journal of the Geological Society*, **173**, 419–437, <https://doi.org/10.1144/jgs2015-129>.
- Franke, W. 2000. The mid-European segment of the Variscides: Tectonostratigraphic units, terrane boundaries and plate tectonic evolution. *Geological Society Special Publication*, **179**, 35–56, <https://doi.org/10.1144/GSL.SP.2000.179.01.05>.
- Franke, W. 2006. The Variscan orogen in Central Europe: Construction and collapse. *Geological Society Memoir*, **32**, 333–343, <https://doi.org/10.1144/GSL.MEM.2006.032.01.20>.
- Gapais, D. 1989. Shear structures within deformed granites: mechanical and thermal indicators. *Geology*, **17**, 1144–1147, [https://doi.org/10.1130/0091-7613\(1989\)017<1144:SSWDGM>2.3.CO;2](https://doi.org/10.1130/0091-7613(1989)017<1144:SSWDGM>2.3.CO;2).
- Garber, J.M. Hacker, B.R. Kylander-Clark, A.R.C. Stearns, M. & Seward, G. 2017. Controls on trace element uptake in metamorphic titanite: Implications for petrochronology. *Journal of Petrology*, **58**, 1031–1057.
- Gibson, R. L & Bickle, M. J. 1994. Thermobarometric constraints on the conditions of metamorphism in the Canigou massif, Pyrenees: implications for Hercynian geothermal gradients. *J Geol Soc*, **15**, 987–997. DOI: 10.1144/gsjgs.151.6.0987.
- Golberg J.-M. (1987) - Le métamorphisme mésozoïque dans la partie orientale des Pyrénées. Relations avec l'évolution de la chaîne au Crétacé - *Thèse de 3e cycle*, 235 p. Montpellier, France.
- Golberg, J.M. & Leyreloup, A.F. 1990. High temperature-low pressure Cretaceous metamorphism related to crustal thinning (Eastern North Pyrenean Zone, France). *Contributions to Mineralogy and Petrology*, **104**, 194–207, <https://doi.org/10.1007/BF00306443>.
- Golberg, J.-M. & Maluski, H. 1988. Données nouvelles et mise au point sur l'âge du métamorphisme pyrénéen. *C.R. Acad. Sci. Paris*,

- Guitard, G. Vielzeuf, D. & Martinez, F. 1996. Métamorphisme hercynien. Synthèse Géologique et Géophysique Des Pyrénées - Edition BRGM - ITGE - Volume 1. 501-584.
- Handy, M.R. & Zingg, A. 1991. The tectonic and rheological evolution of an attenuated cross-section of the continental crust: Ivrea crustal section, southern Alps, northwestern Italy and southern Switzerland. *Geological Society of America Bulletin*, **103**, 236-253.
- Hart, N. R. Stockli, D. F. & Hayman N. W. 2016. Provenance evolution during progressive rifting and hyperextension using bedrock and detrital zircon U-Pb geochronology, Mauléon Basin, western Pyrenees. *Geosphere*, **12**(4), 1166–1186.
- Hart, N.R. Stockli, D.F. Lavier, L.L. & Hayman, N.W. 2017. Thermal evolution of a hyperextended rift basin, Mauléon Basin, western Pyrenees. *Tectonics*, **36**, 1103–1128, <https://doi.org/10.1002/2016TC004365>.
- Hawthorne, F.C. Oberti, R. Harlow, G.E. Maresch, W. V, Martin, R.F. Schumacher, J.C. & Welch, M.D. 2012. Nomenclature of the amphibole supergroup. *American Mineralogist*, **97**, 2031–2048, <https://doi.org/10.2138/am.2012.4276>.
- Hayden, L.A. Watson, E.B. & Wark, D.A. 2008. A thermobarometer for sphene (titanite). *Contributions to Mineralogy and Petrology*, **155**, 529–540, <https://doi.org/10.1007/s00410-007-0256-y>.
- Heaman, L.M. 2009. The application of U-Pb geochronology to mafic, ultramafic and alkaline rocks: An evaluation of three mineral standards. *Chemical Geology*, **261**, 43–52, <https://doi.org/10.1016/j.chemgeo.2008.10.021>.
- Henk, A. Franz, L. Teufel, S. & Oncken, O. 1997. Magmatic underplating, extension, and crustal reequilibration: insights from a cross-section through the Ivrea Zone and Strona-Ceneri Zone, northern Italy. *Journal of Geology*, **105**, 367-377.
- Henry, D.J. Guidotti, C.V. & Thomson, J.A. 2005. The Ti-saturation surface for low-to-medium pressure metapelitic biotites: Implications for geothermometry and Ti-substitution mechanisms. *Am. Mineral.* **90**(2-3), 316-328.
- Hiess, J. Condon, D.J. McLean, N. & Noble, S.R. 2012. 238U/235U systematics in terrestrial uranium-bearing minerals. *Science*, **335**, 1610–1614, <https://doi.org/10.1126/science.1215507>.
- Holder, R.M. Hacker, B.R. Seward, G.G.E. & Kylander-Clark, A.R.C. 2019. Interpreting titanite U-Pb dates and Zr thermobarometry in high-grade rocks: Empirical constraints on elemental diffusivities of Pb, Al, Fe, Zr, Nb, and Ce. *Contributions to Mineralogy and Petrology*, **174**, 1-19.
- Holland, T. & Blundy, J. 1994. Non-ideal interactions in calcic amphiboles and their bearing on amphibole-plagioclase thermometry. *Contributions to Mineralogy and Petrology*, **116**, 433–447, <https://doi.org/10.1007/BF00310910>.
- Horstwood, M.S.A. Košler, J. Gehrels, G. Jackson, S.E. McLean, N.M. Paton, C. Pearson, N.J. Sircombe, K. Sylvester, P. Vermeesch,

- P. Bowring, J.F. Condon, D.J. & Schoene, B. 2016. Community-Derived Standards for LA-ICP-MS U-(Th-)Pb Geochronology – Uncertainty Propagation, Age Interpretation and Data Reporting. *Geostandards and Geoanalytical Research*, **40**, 311-332, doi: 10.1111/j.1751-908X.2016.00379.x.
- Kydonakis, K. Kostopoulos, D. Poujol, M. Brun, J.-P. Papanikolaou, D. & Paquette, J.-L. 2014. The dispersal of the Gondwana Superfan System in the eastern Mediterranean: New insights from detrital zircon geochronology. *Gondwana Research*, **25**(3), 1230-1241, <https://dx.doi.org/10.1016/j.gr.2013.05.009>.
- Jackson, S.E. Pearson, N.J. Griffin, W.L. & Belousova, E.A. 2004. The application of laser ablation-inductively coupled plasma-mass spectrometry to in situ U-Pb zircon geochronology. *Chemical Geology*, **211**, 47–69, <https://doi.org/10.1016/j.chemgeo.2004.06.017>.
- Jammes, S. Manatschal, G. Lavier, L. & Masini, E. 2009. Tectonosedimentary evolution related to extreme crustal thinning ahead of a propagating ocean: Example of the western Pyrenees. *Tectonics*, **28**, <https://doi.org/10.1029/2008TC002406>.
- Jarosewich, E. & Boatner, L.A. 1991. Rare-Earth Element Reference Samples for Electron Microprobe Analysis. *Geostandards and Geoanalytical Research*, **15**, 397–399, <https://doi.org/10.1111/j.1751-908X.1991.tb00115.x>.
- Jourdon, A. Le Pourhiet, L. Mouthereau, F. & Masini, E. 2019. Role of rift maturity on the architecture and shortening distribution in mountain belts. *Earth and Planetary Science Letters*, **512**, 89–99, <https://doi.org/10.1016/j.epsl.2019.01.057>.
- Kohn, M.J. 2017. Titanite petrochronology. *Reviews in Mineralogy & Geochemistry*, **83**, 419-441.
- Lagabrielle, Y. Labaume, P. & De Saint Blanquat, M. 2010. Mantle exhumation, crustal denudation, and gravity tectonics during Cretaceous rifting in the Pyrenean realm (SW Europe): Insights from the geological setting of the Iherzolite bodies. *Tectonics*, **29**, 1–26, <https://doi.org/10.1029/2009TC002588>.
- Lagabrielle, Y. Clerc, C. *et al.* 2016. Very high geothermal gradient during mantle exhumation recorded in mylonitic marbles and carbonate breccias from a Mesozoic Pyrenean palaeomargin (Lherz area, North Pyrenean Zone, France). *Comptes Rendus - Geoscience*, **348**, 290–300, <https://doi.org/10.1016/j.crte.2015.11.004>.
- Lagabrielle, Y. Asti, R. *et al.* 2020. A review of cretaceous smooth-slopes extensional basins along the Iberia-Eurasia plate boundary: How pre-rift salt controls the modes of continental rifting and mantle exhumation. *Earth-Science Reviews*, **201**, 103071, <https://doi.org/10.1016/j.earscirev.2019.103071>.
- Laurent, O. Couzinié, S. Zeh, A. Vanderhaeghe, O. Moyen, J.-F. Villaros, A. Gardien, V. & Chelle-Michou, C. 2017. Protracted, coeval crust and mantle melting during Variscan late-orogenic evolution: U-Pb dating in the eastern French Massif Central. *International Journal of Earth Sciences*, **106**, 421-451. <https://doi.org/10.1007/s00531-016-1434-9>

- Le Roux, V. Bodinier, J.L. Tommasi, A. Alard, O. Dautria, J.M. Vauchez, A. & Riches, A.J.V. 2007. The Lherz spinel lherzolite: Refertilized rather than pristine mantle. *Earth and Planetary Science Letters*, **259**, 599–612, <https://doi.org/10.1016/j.epsl.2007.05.026>.
- Leake, B.E. Woolley, A.R. *et al.* 1997. Nomenclature of amphiboles; report of the subcommittee on amphiboles of the International Mineralogical Association, Commission on New Minerals and Mineral Names. *The Canadian Mineralogist*, **35** (1), 219–246.
- Leake, B.E. Woolley, A.R. *et al.* 2004. Nomenclature of amphiboles: Additions and revisions to the International Mineralogical Association's amphibole nomenclature. *American Mineralogist*, **89**, 883–887, <https://doi.org/10.1180/0026461046810182>.
- Lemirre, B. 2018. Origine et développement de la thermicité dans les Pyrénées varisques. PhD thesis, Univ. Paul Sabatier, Toulouse, France.
- Lemirre, B. Cochelin, B. Duchene, S. de Saint Blanquat, M. & Poujol, M. 2019. Origin and duration of late orogenic magmatism in the foreland of the Variscan belt (Lesponne-Chiroulet-Neouvielle area, French Pyrenees). *Lithos*, **336-337**, 183–201. doi: 10.1016/j.lithos.2019.03.037
- Locock, A.J. 2014. An Excel spreadsheet to classify chemical analyses of amphiboles following the IMA 2012 recommendations. *Computers and Geosciences*, **62**, 1–11, <https://doi.org/10.1016/j.cageo.2013.09.011>.
- Lucci, F. Della Ventura, G. Conte, A. Nazzari, M. & Scarlato, P. 2018. Naturally occurring asbestos (NOA) in granitoid rocks, a case study from Sardinia (Italy). *Minerals*, **8**(10), 442.
- Ludwig, K.R. 1998. On the treatment of concordant uranium-lead ages. *Geochimica et Cosmochimica Acta*, **62**, 665–676, [https://doi.org/10.1016/S0016-7037\(98\)00059-3](https://doi.org/10.1016/S0016-7037(98)00059-3).
- Malavieille, J. Guihot, P. Costa, S. Lardeaux, J.M. & Gardien, V. 1990. Collapse of the thickened Variscan crust in the French Massif Central: Mont Pilat extensional shear zone and St. Etienne Late Carboniferous basin. *Tectonophysics*, **177**, 139–149, [https://doi.org/10.1016/0040-1951\(90\)90278-G](https://doi.org/10.1016/0040-1951(90)90278-G).
- Masini, E. Manatschal, G. Tugend, J. Mohn, G. & Flament, J.M. 2014. The tectono-sedimentary evolution of a hyper-extended rift basin: The example of the Arzacq-Mauléon rift system (Western Pyrenees, SW France). *International Journal of Earth Sciences*, **103**, 1569–1596, <https://doi.org/10.1007/s00531-014-1023-8>.
- Matte, P. 2001. The Variscan collage and orogeny (480–290 Ma) and the tectonic definition of the Armorica microplate: a review. *Terra Nova*, **13**, 122–128.
- Mezger, J. E. 2005. Comparison of the western Aston–Hospitalet and the Bossòst domes: Evidence for polymetamorphism and its implications for the Variscan tectonic evolution of the Axial Zone of the Pyrenees. *Journal of the Virtual Explorer*, **19**,

<https://doi.org/10.3809/jvirtex.2005.00122>

- Mezger, J. E. & Régnier, J.-L. 2016. Stable staurolite–cordierite assemblages in K-poor metapelitic schists in Aston and Hospitalet gneiss domes of the central Pyrenees (France, Andorra). *Journal of Metamorphic Geology*, **34**, 167–190, <https://doi.org/10.1111/jmg.12177>
- Mohn, G. Manatschal, G. Beltrando, M. Masini, E. & Kuszniir, N. 2012. Necking of continental crust in magma-poor rifted margins: evidence from fossil Alpine Tethys margins. *Tectonics*, **31**, doi:10.1029/2011TC002961
- Monchoux, P. 1970. Les lherzolites pyrénéennes: contribution à l'étude de leur minéralogie, de leur genèse et de leurs transformations - *Ph.D. thesis*, 180 pp. Univ. of Toulouse, Toulouse, France.
- Montigny, R. Azambre, B. Rossy, M. & Thuizat, R. 1986. K-Ar Study of cretaceous magmatism and metamorphism in the pyrenees: Age and length of rotation of the liberian Peninsula. *Tectonophysics*, **129**, 257–273, [https://doi.org/10.1016/0040-1951\(86\)90255-6](https://doi.org/10.1016/0040-1951(86)90255-6).
- Muñoz, J.A. 1992. Evolution of a continental collision belt: ECORS-Pyrenees crustal balanced cross-section. *In: Thrust Tectonics*. Springer Netherlands, 235–246. https://doi.org/10.1007/978-94-011-3066-0_21.
- Mutch, E.J.F. Blundy, J.D. Tattitch, B.C. Cooper, F.J. & Brooker, R.A. 2016. An experimental study of amphibole stability in low-pressure granitic magmas and a revised Al-in-hornblende geobarometer. *Contributions to Mineralogy and Petrology*, **171**, 1–27, <https://doi.org/10.1007/s00410-016-1298-9>.
- Newman, J. Lamb, W.M. Drury, M.R. & Vissers, R.L.M. 1999. Deformation processes in a peridotite shear zone: Reaction-softening by an H₂O-deficient, continuous net transfer reaction. *Tectonophysics*, **303**, 193–222, [https://doi.org/10.1016/S0040-1951\(98\)00259-5](https://doi.org/10.1016/S0040-1951(98)00259-5).
- Nirrengarten, M. Manatschal, G. Tugend, J. Kuszniir, N. & Sauter, D. 2018. Kinematic Evolution of the Southern North Atlantic: Implications for the Formation of Hyperextended Rift Systems. *Tectonics*, **37**, 89–118, <https://doi.org/10.1002/2017TC004495>.
- Oldum, M. L. & Sockli, D. F. 2020. Geochronologic constraints on deformation and metasomatism along an exhumed mylonitic shear zone using apatite U-Pb, geochemistry, and microtextural analysis. *Earth and Planetary Science Letters*, **538**, 116177. <https://doi.org/10.1016/j.epsl.2020.116177>
- Olivet, J. 1996. La cinématique de la plaque ibérique. **20**, 131–195.
- Olivier, P. Gleizes, G. Paquette, J.-L. Muñoz Sáez, C. 2008. Structure and U-Pb dating of the Saint-Arnac pluton and the Ansignan charnockite (Agly Massif): a cross-section from the upper to the middle crust of the Variscan Eastern Pyrenees. *Journal of the Geological Society*, **165**, 141-152.

- Passchier, C.W. & Trouw, R.A.J. 2005. *Microtectonics*. Springer Berlin Heidelberg, <https://doi.org/10.1007/3-540-29359-0>.
- Paton, C. Woodhead, J.D. Hellstrom, J.C. Hergt, J.M. Greig, A. & Maas, R. 2010. Improved laser ablation U-Pb zircon geochronology through robust downhole fractionation correction. *Geochemistry, Geophysics, Geosystems*, **11**, <https://doi.org/10.1029/2009GC002618>@10.1002/(ISSN)1525-2027.EARTHTIME1.
- Paton, C. Hellstrom, J. Paul, B. Woodhead, J. & Hergt, J. 2011. Lolite: Freeware for the visualisation and processing of mass spectrometric data. *Journal of Analytical Atomic Spectrometry*, **26**, 2508–2518, <https://doi.org/10.1039/c1ja10172b>.
- Pedersen, R.B. Dunning, G.R. & Robins, B. 1989. U-Pb ages of nepheline syenite pegmatites from the Seiland Magmatic Province, N Norway. *The Caledonide geology of Scandinavia*, 3–8, https://doi.org/10.1007/978-94-009-2549-6_1.
- Péron-Pinvidic, G. & Manatschal, G. 2009. The final rifting evolution at deep magma-poor passive margins from Iberia-Newfoundland: A new point of view. *Int. J. Earth Sci.*, **98**, 1581–1597, doi:10.1007/s00531-008-0337-9
- Petrus, J.A. & Kamber, B.S. 2012. VizualAge: A Novel Approach to Laser Ablation ICP-MS U-Pb Geochronology Data Reduction. *Geostandards and Geoanalytical Research*, **36**, 247–270, <https://doi.org/10.1111/j.1751-908X.2012.00158.x>.
- Pin, C. 1989. Essai sur la chronologie et l'évolution géodynamique de la chaîne hercynienne d'Europe. *Thèse Sciences de la Terre*. Université Blaise Pascal - Clermont-Ferrand II, tel-01001861
- Pin, C. & Vielzeuf, D. 1983. Granulites and related rocks in variscan median Europe: A dualistic interpretation. *Tectonophysics*, **93**, 47–74, [https://doi.org/10.1016/0040-1951\(83\)90233-0](https://doi.org/10.1016/0040-1951(83)90233-0).
- Postaire, B. 1983. Systématique Pb commun et U–Pb sur zircons: Applications aux roches de haut grade métamorphique impliquées dans la chaîne hercynienne (Europe de l'Ouest) et aux granulites de Laponie (Finlande). *Bulletin de la Société Géologique et Minéralogique de Bretagne*, **15**, 29–72.
- Pouchou, J.L. & Pichoir, F. 1984. ANALYSE D'ÉCHANTILLONS STRATIFIÉS À LA MICROSONDE ÉLECTRONIQUE. *Le Journal de Physique Colloques*, **45**, C2-47-C2-50, <https://doi.org/10.1051/jphyscol:1984212>.
- Puigdefàbregas, C. & Souquet, P. 1986. Tecto-sedimentary cycles and depositional sequences of the Mesozoic and Tertiary from the Pyrenees. *Tectonophysics*, **129**, 173–203, [https://doi.org/10.1016/0040-1951\(86\)90251-9](https://doi.org/10.1016/0040-1951(86)90251-9).
- Quick, J.E. Sinigoi, S. & Mayer, A. 1995. Emplacement of mantle peridotite in the lower continental crust, IVZ, northwest Italy. *Geology*, **23/8**, 739-742.
- Quick, J.E. Sinigoi, S. Peressini, G. Demarchi, G. Wooden, J.L. & Sbisà, A. 2009. Magmatic plumbing of a large Permian caldera exposed to a depth of 25 km. *Geology*, **37**, 603-606.

- Rivalenti, G. & Mazzucchelli, M. 2000. Interaction of mantle derived magmas and crust in the IVZ and the Ivrea mantle peridotites. In: Ranalli G., Ricci C.A. & Trommsdorff V. (eds) - "Crust Mantle Interactions, Proceedings of the International School Earth and Planetary Sciences", 153-198.
- Rosenberg, C.L. & Stünitz, H. 2003. Deformation and recrystallization of plagioclase along a temperature gradient: An example from the Bergell tonalite. *Journal of Structural Geology*, **25**, 389–408, [https://doi.org/10.1016/S0191-8141\(02\)00036-6](https://doi.org/10.1016/S0191-8141(02)00036-6).
- Rossetti, F. Nozaem, R. Lucci, F. Vignaroli, G. Gerdes, A. Nasrabadi, M. & Theye, T. 2015. Tectonic setting and geochronology of the Cadomian (Ediacaran-Cambrian) magmatism in central Iran, Kuh-e-Sarhangi region (NW Lut Block). *J. Asian Earth Sci.* **102**, 24–44.
- Rossetti, F. Asti, R. Faccenna, C. Gerdes, A. Lucci, F. & Theye, T. 2017. Magmatism and crustal extension: Constraining activation of the ductile shearing along the Gediz detachment, Menderes Massif (western Turkey). *Lithos*, **282–283**, 145–162, <https://doi.org/10.1016/j.lithos.2017.03.003>.
- Roure, F. Choukroune, P. *et al.* 1989. Ecors deep seismic data and balanced cross sections: Geometric constraints on the evolution of the Pyrenees. *Tectonics*, **8**, 41–50, <https://doi.org/10.1029/TC008i001p00041>.
- Rubatto, D. 2002. Zircon trace element geochemistry: partitioning with garnet and the link between U–Pb ages and metamorphism. *Chemical Geology*, **184**, 123–138. [https://doi.org/10.1016/S0009-2541\(01\)00355-2](https://doi.org/10.1016/S0009-2541(01)00355-2)
- Rutter, E.H. Khazanehdari, J. Brodie, K.H. Blundell, D.J. & Waltham, D.A. 1999. Synthetic seismic reflection profile through the Ivrea Zone-Serie dei Laghi continental crustal section, northwestern Italy. *Geology*, **27**, 79-82.
- Saspiturry, N. Cochelin, B. *et al.* 2019. Tectono-sedimentary evolution of a rift system controlled by Permian post-orogenic extension and metamorphic core complex formation (Bidarray Basin and Ursuya dome, Western Pyrenees). *Tectonophysics*, **768**, 228180, <https://doi.org/10.1016/j.tecto.2019.228180>.
- Saspiturry, N. Lahfid, A. Baudin, T. Guillou-Frottier, L. Razin, P. Issautier, B. Le Bayon, B. Serrano, O. Lagabrielle, Y. & Corre, B. 2020. Paleogeothermal gradients across an inverted hyperextended rift system: Example of the mauléon fossil rift (Western Pyrenees). *Tectonics*, **39**(10), 1–36. <https://doi.org/10.1029/2020TC006206>
- Saspiturry, N. Issautier, B. Razin, P. Baudin, T. Asti, R. Lagabrielle, Y. *et al.* 2021. Review of Iberia-Eurasia plate-boundary basins: role of sedimentary burial on depth-dependent continental crust ductile thinning during rifting and continental breakup. *Basin Research*, **33**, 1626–1661. DOI: 10.1111/bre.12529
- Schmidt, M.W. 1992. Amphibole composition in tonalite as a function of pressure: an experimental calibration of the Al-in-hornblende barometer. *Contributions to Mineralogy and Petrology*, **110**, 304–310, <https://doi.org/10.1007/BF00310745>.

- Schmidt, M.W. & Poli, S. 2004. Magmatic epidote. *Reviews in Mineralogy and Geochemistry*, **56**, 399–430, <https://doi.org/10.2138/gsrmg.56.1.399>.
- Siron, G. Goncalves, P. Marquer, D. Trap, P. Paquette, J.L. Vanandois, J. 2020. Contribution of magmatism, partial melting buffering and localized crustal thinning on the late-Variscan thermal structure of the Agly massif (French Pyrenees). *Journal of Metamorphic Geology*, doi: 10.1111/JMG.12549.
- Sláma, J. Košler, J. *et al.* 2008. Plešovice zircon - A new natural reference material for U-Pb and Hf isotopic microanalysis. *Chemical Geology*, **249**, 1–35, <https://doi.org/10.1016/j.chemgeo.2007.11.005>.
- Stacey, J.S. & Kramers, J.D. 1975. Approximation of terrestrial lead isotope evolution by a two-stage model. *Earth and Planetary Science Letters*, **26**, 207–221, [https://doi.org/10.1016/0012-821X\(75\)90088-6](https://doi.org/10.1016/0012-821X(75)90088-6).
- Teixell, A. Labaume, P. Ayarza, P. Espurt, N. de Saint Blanquat, M. & Lagabrielle, Y. 2018. Crustal structure and evolution of the Pyrenean-Cantabrian belt: A review and new interpretations from recent concepts and data. *Tectonophysics*, **724–725**, 146–170, <https://doi.org/10.1016/j.tecto.2018.01.009>.
- Ternet, Y. Colchen, M. Debroas, E.J. Azambreb, Debon, F., Bouchez, J.L. Gleizesg, Leblanc, D. Bakalowicz, M. Jauziong, Mangina, Soula, J.C. 1997. Notice explicative, Carte géol. France (1/50 000), feuille Aulus-les-Bains (1086). Orléans : BRGM, 146 p.
- Triboulet, C. Guitard, G. Katona, I. & Navidad, M. 2005. Évolution pression–température des amphibolites de la zone axiale au cours du métamorphisme hercynien des Pyrénées orientales. *Comptes Rendus Géoscience*, **337**, 1244–1249, <https://doi.org/10.1016/j.crte.2005.06.011>
- Tugend, J. Manatschal, G. Kuszniir, N.J. Masini, E. Mohn, G. & Thinon, I. 2014. Formation and deformation of hyperextended rift systems: Insights from rift domain mapping in the Bay of Biscay-Pyrenees. *Tectonics*, **33**, 1239–1276, <https://doi.org/10.1002/2014TC003529>.
- Tullis, J. & Yund, R.A. 1991. Diffusion creep in feldspar aggregates: experimental evidence. *Journal of Structural Geology*, **13**, 987–1000, [https://doi.org/10.1016/0191-8141\(91\)90051-J](https://doi.org/10.1016/0191-8141(91)90051-J).
- Vacherat, A. Mouthereau, F. *et al.* 2014. Thermal imprint of rift-related processes in orogens as recorded in the Pyrenees. *Earth and Planetary Science Letters*, **408**, 296–306, <https://doi.org/10.1016/j.epsl.2014.10.014>.
- Van Den Driessche, J. & Brun, J.P. 1991. Tectonic evolution of the Montagne Noire (French Massif Central): a model of extensional gneiss dome. *Geodinamica Acta*, **5**, 85–99, <https://doi.org/10.1080/09853111.1992.11105221>.
- Vergés, J. & García-Senz, J. M. 2001. Mesozoic Evolution and Cenozoic Inversion of the Pyrenean Rift. In Ziegler, P. A. Cavazza, W. Robertson, A. H. F. & Crasquin-Soleau, S. eds. *Peri-Tethys Memoir 6: Pery-Tethyan Rift/Wrench Basins and Passive Margins*.

Mémoires Muséum National d'Histoire Naturelle, **186**, 187-212.

- Vergés, J. Fernández, M. & Martínez, A. 2002. The Pyrenean orogen: pre-, syn-, and post-collisional evolution. *Journal of the Virtual Explorer*, **08**, 55–74, <https://doi.org/10.3809/jvirtex.2002.00058>.
- Vermeesch, P. 2018. IsoplotR: A free and open toolbox for geochronology. *Geoscience Frontiers*, **9**, 1479–1493, <https://doi.org/10.1016/j.gsf.2018.04.001>.
- Vielzeuf, D. 1979. Les paragneiss granulitiques de Lers et Saleix (Ariège), les réactions minéralogiques témoins de leur rétrogenèse. *C. R. Acad. Sci. Paris*, **289**, 5-8.
- Vielzeuf, D. 1980a. Pétrologie des écaillés granulitiques de la région de Lherz (Ariège-Zone Nord-Pyrénéenne). Introduction à l'étude expérimentale de l'association grenat (Alm-Pyr) -feldspath potassique. *Thèse 3ème cycle*, 219 pp. Clermont-Ferrand, France.
- Vielzeuf, D. 1980b. Existence d'un fragment de « complexe stratifié » (pyriclasites et anorthosites) associé à la série granulitique du port de Saleix (Pyrénées ariégeoises). *Bulletin de Minéralogie*, **103**, 287–296, <https://doi.org/10.3406/bulmi.1980.7406>.
- Vielzeuf D. 1984. Relations de phase dans le faciès granulite et implications géodynamiques. L'exemple des granulites des Pyrénées. *Thèse Sci.* 288 pp. Univ. Clermont II, France.
- Vielzeuf, D. & Kornprobst, J. 1984. 'Crustal splitting and the emplacement of Pyrenean lherzolites and granulites'-A reply to M.W. Fischer. *Earth and Planetary Science Letters*, **70**, 439–443, [https://doi.org/10.1016/0012-821X\(84\)90028-1](https://doi.org/10.1016/0012-821X(84)90028-1).
- Vilà, M. Pin, C. Liesa, M. & Enrique, P. 2007. LP-HT metamorphism in a late orogenic transpressional setting, Albera Massif, NE Iberia: implications for the geodynamic evolution of the Variscan Pyrenees. *Journal of Metamorphic Geology*, **25**, 321–347, <https://doi.org/10.1111/j.1525-1314.2007.00698.x>
- Viskupic, K. Hodges, K.V. & Bowring, S.A. 2005. Timescales of melt generation and the thermal evolution of the Himalayan metamorphic core, Everest region, eastern Nepal. *Contrib Mineral Petrol*, **149**, 1–21. <https://doi.org/10.1007/s00410-004-0628-5>
- Vissers, R.L.M. 1992. Variscan extension in the Pyrenees. *Tectonics*, **11**, 1369–1384, <https://doi.org/10.1029/92TC00823>.
- Walters, J.B. & Kohn, M.J. 2017. Protracted thrusting followed by late rapid cooling of the Greater Himalayan Sequence, Annapurna Himalaya, Central Nepal: Insights from titanite petrochronology. *Journal of Metamorphic Geology*, **35**(8), 897–917, [doi:10.1111/jmg.12260](https://doi.org/10.1111/jmg.12260)
- Whitney, D.L. & Evans, B.W. 2010. Abbreviations for names of rock-forming minerals. *American Mineralogist*, **95**, 185–187, <https://doi.org/10.2138/am.2010.3371>.
- Zen, E.A. & Hammarstrom, J.M. 1984. Magmatic epidote and its petrologic significance. *Geology*, **12**, 515–518,

[https://doi.org/10.1130/0091-7613\(1984\)12<515:MEAIPS>2.0.CO;2](https://doi.org/10.1130/0091-7613(1984)12<515:MEAIPS>2.0.CO;2).

Ziegler, P.A. & Dèzes, P. 2006. Crustal evolution of Western and Central Europe. *Geological Society Memoir*, **32**, 43–56,
<https://doi.org/10.1144/GSL.MEM.2006.032.01.03>.

Ziegler, P.A. Schumacher, M.E. Dèzes, P. van Wees, J.D. & Cloetingh, S. 2004. Post-Variscan evolution of the lithosphere in the Rhine Graben area: Constraints from subsidence modelling. *Geological Society Special Publication*, **223**, 289–317,
<https://doi.org/10.1144/GSL.SP.2004.223.01.13>.

Ziegler, P.A. Schumacher, M.E. Dèzes, P. van Wees, J.D. & Cloetingh, S. 2006. Post-Variscan evolution of the lithosphere in the area of the European Cenozoic Rift System. *Geological Society Memoir*, **32**, 97–112,
<https://doi.org/10.1144/GSL.MEM.2006.032.01.06>.

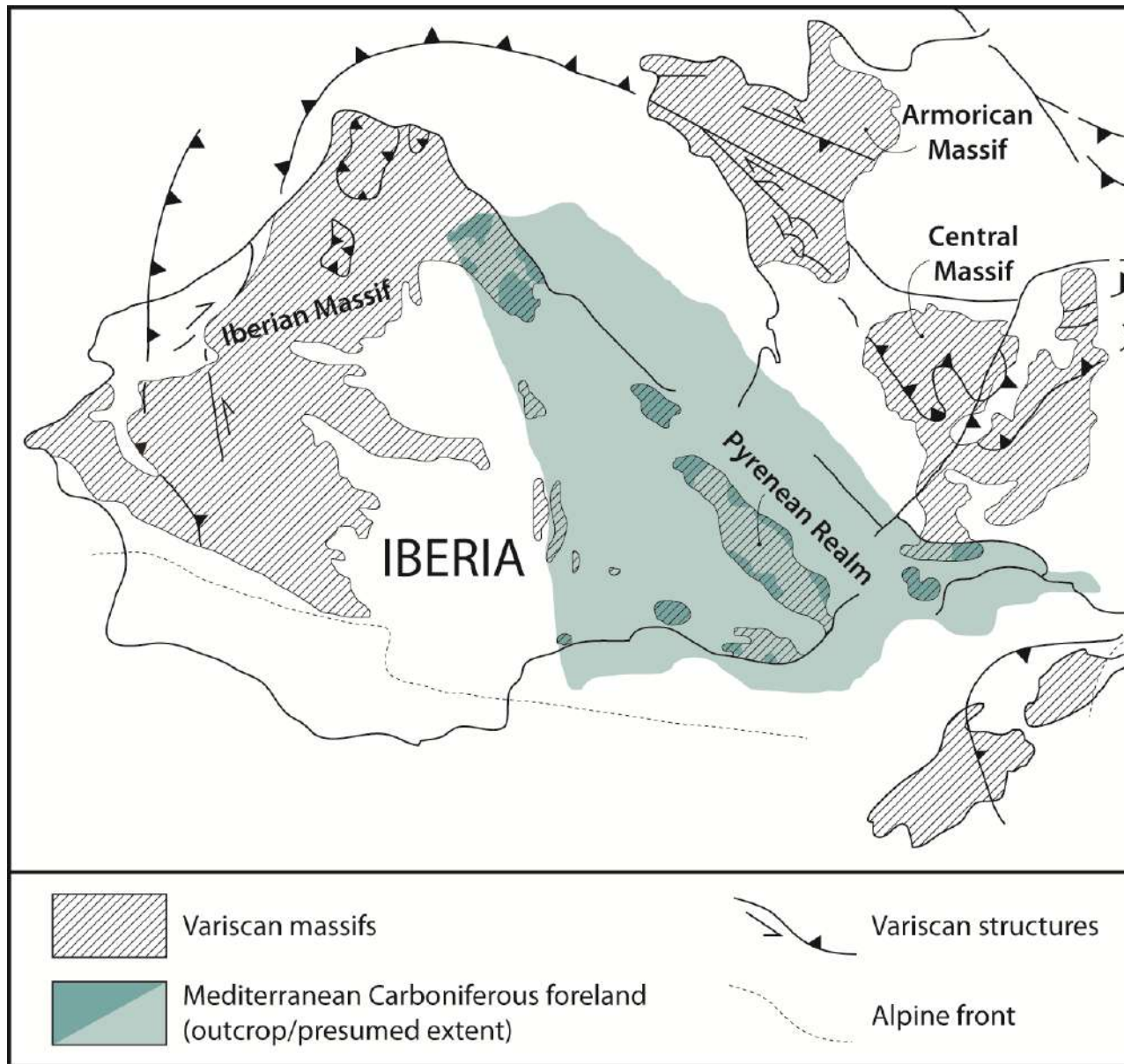


Fig. 1: Structural map of the western European Variscides (on a Permian plate configuration) with representation of the Mediterranean Carboniferous foreland basin (in blue). Redrawn and modified after Franke (2000, 2006) and Matte (2001).

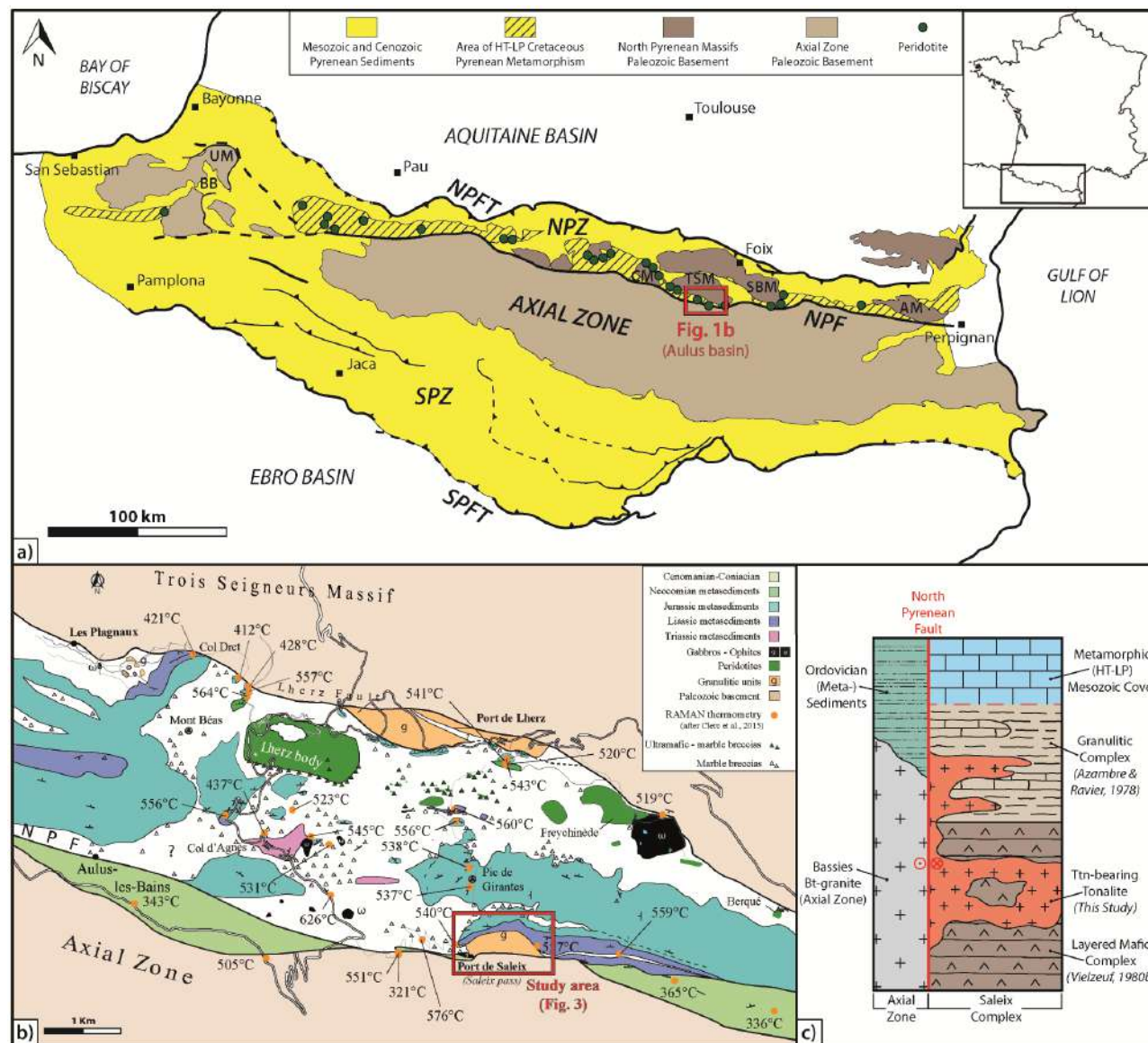


Fig. 2: (a) Synthetic structural map of the Pyrenean belt with location of the main outcropping ultramafic bodies and distribution of the terranes affected by the Cretaceous HT/LP metamorphism (redrawn and modified after Corre et al. 2018). Acronyms: AM, Agly massif; BB, Bidarray basin; CM, Castillon massif; NPFT, North Pyrenean Frontal Thrust; NPZ, North Pyrenean Zone; SBM, Saint Barthélémy massif; SPFT, South Pyrenean Frontal Thrust; SPZ, South Pyrenean Zone; TSM, Trois Seigneurs massif; UM, Ursuya massif. (b) Geological map of the central part of the Aulus Basin (modified after Lagabrielle et al. 2016) with location of the study area. (c) Schematic representation of the tectono-stratigraphic relationships between the different lithologies in the Saleix Complex.

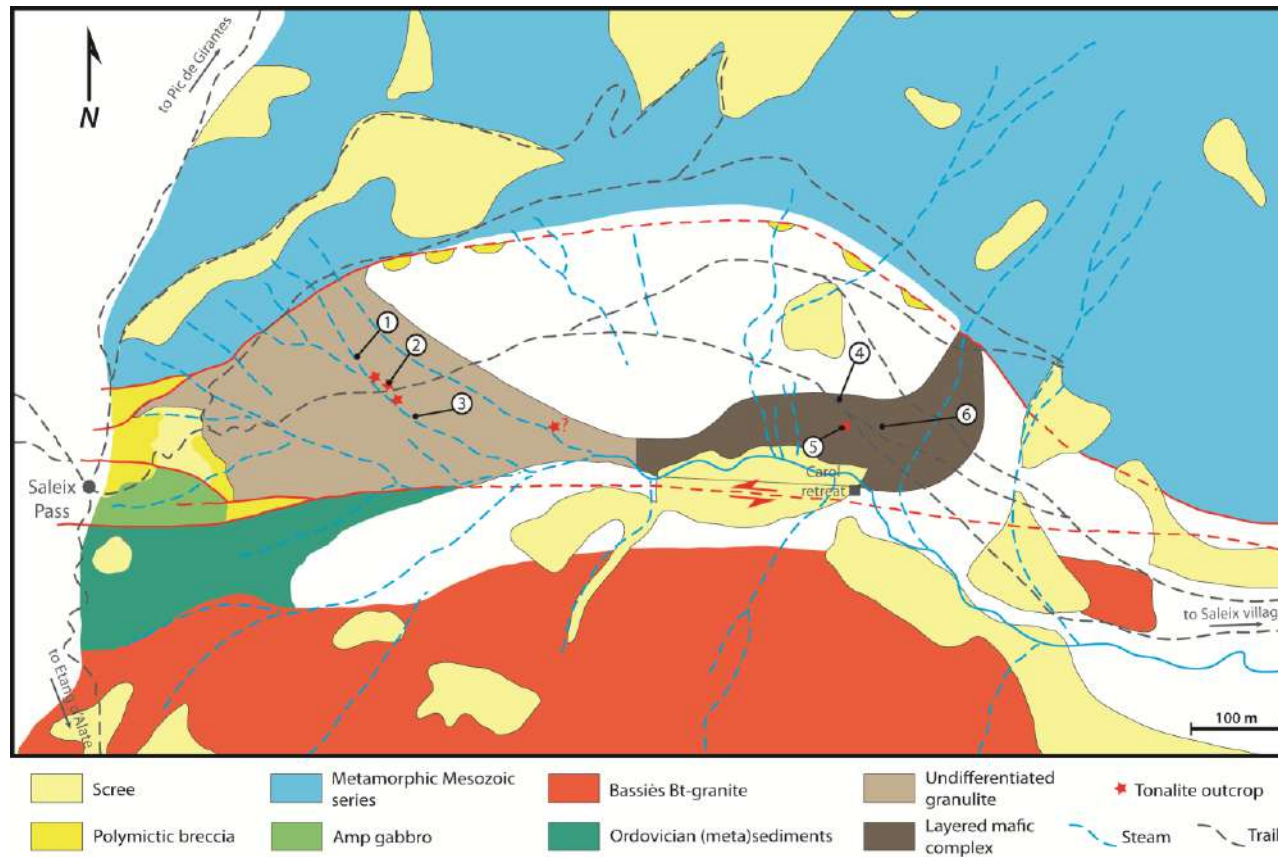


Fig. 3: Simplified geological map of the Saleix Massif redrawn and modified after Vielzeuf (1980a). Numbers in circles indicate sites of structural analysis reported in figure 6. Samples dated in this study (SAL D2 and SAL E) were collected at site 2.



Fig. 4: Some examples of granulitic lithotypes outcropping in the Saleix Massif. **(a, b)** Sub-vertical tectonic foliation in granulitic paragneiss (site 1 on Fig. 3). **(c)** Steeply dipping, E-W striking tectonic foliation in granulitic gneiss (site 3 in Fig. 3). **(d)** Mafic charnockite boudin (dark brown) in granulites (light brown; close to site 3 in Fig. 3). **(e, f)** Sub-vertical E-W striking tectonic foliation in the layered mafic complex (mafic charnockites), eastern part of the Saleix Massif (site 6 in Fig. 3; plane view).



Fig. 5: Structures of the Saleix tonalites at the outcrop scale. (a) Magmatic (primary) foliation in the Saleix tonalite (left side) overprinted by a sub-vertical solid-state tectonic (mylonitic) foliation (right side); plane view. (b) Example of S-C fabric developed in the Saleix Complex with the shear foliation defined by metamorphic amphibole locally surrounding porphyroclastic magmatic plagioclase;

plane view. (c) Example of syn-metamorphic amphibole-bearing shear band in the Saleix tonalites. Pictures a, b and c are taken from the eastern part of the Saleix Massif (site 5 in Fig. 3), where the tonalites intrude the mafic complex. (d) Example of intensely foliated tonalite, with sub-vertical E-W striking foliation (granulitic complex in the western part of the massif; site 2 in Fig. 3).

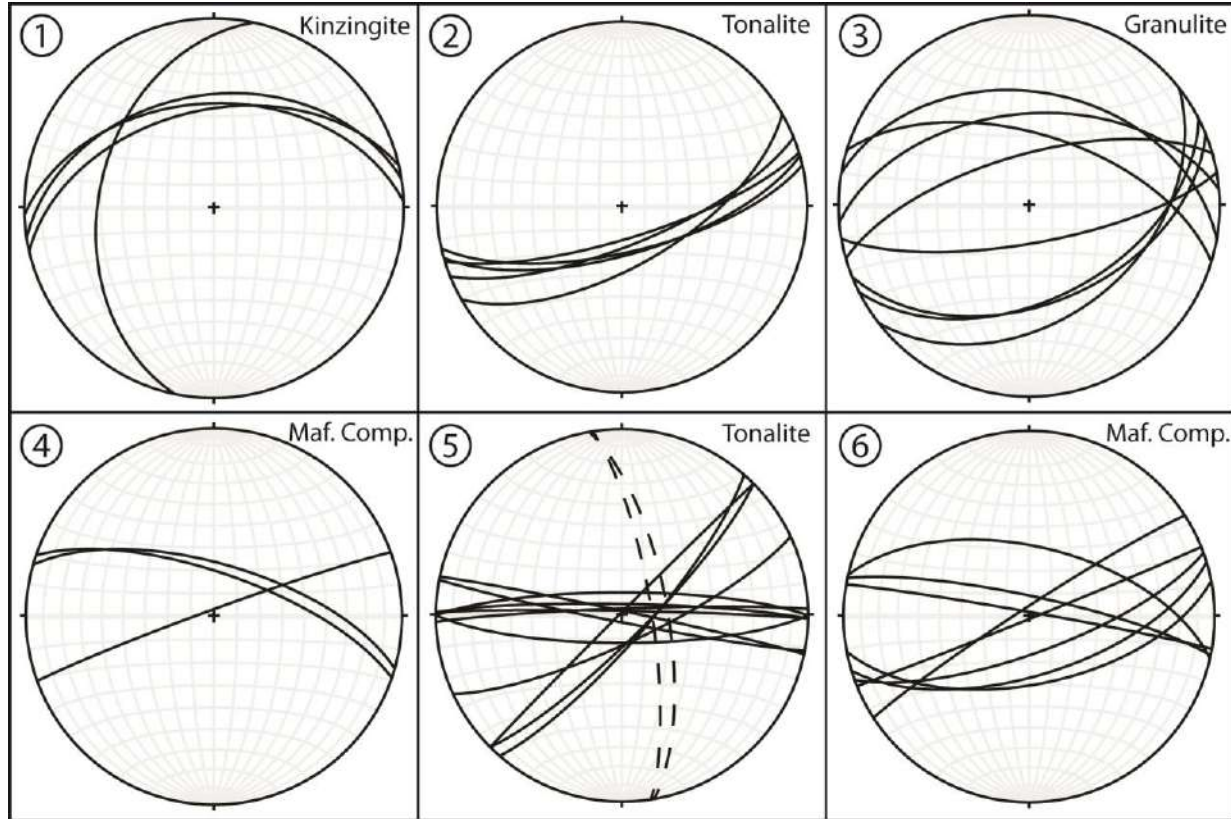


Fig. 6: Equal area stereoplots (Schmidt net, lower hemisphere) showing the attitude of the magmatic (dashed lines in stereoplot#5) and syn-metamorphic tectonic (solid lines) foliations in the Saleix Complex. Numbers on the top left of the stereonets refer to locations of structural analysis sites reported in figure 3.

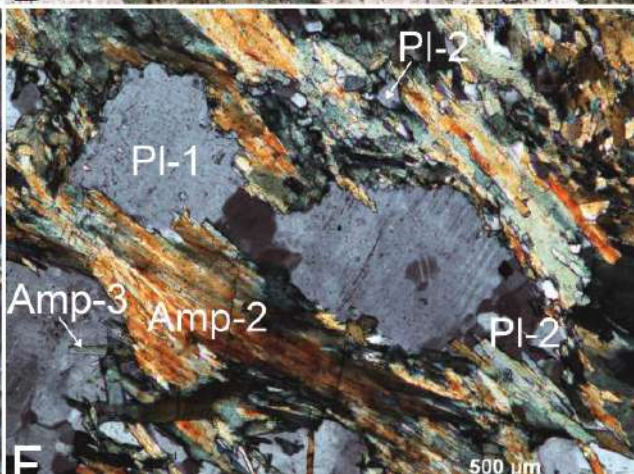
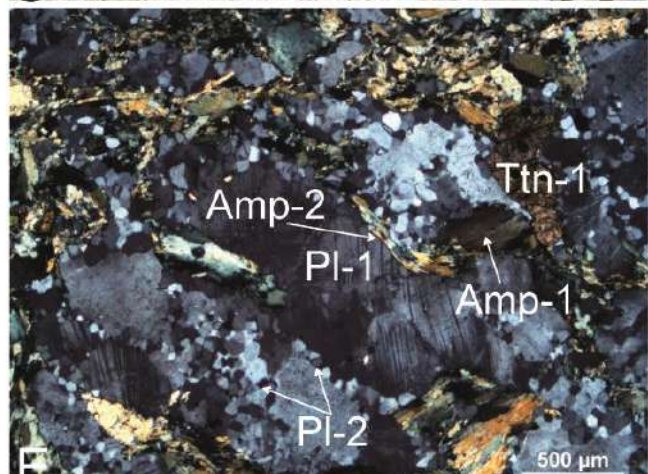
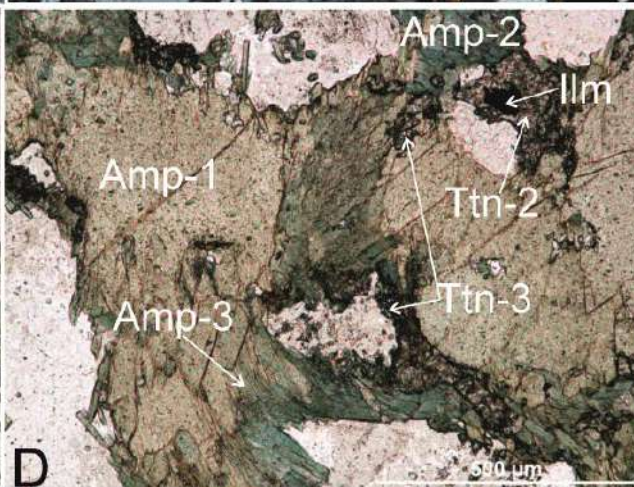
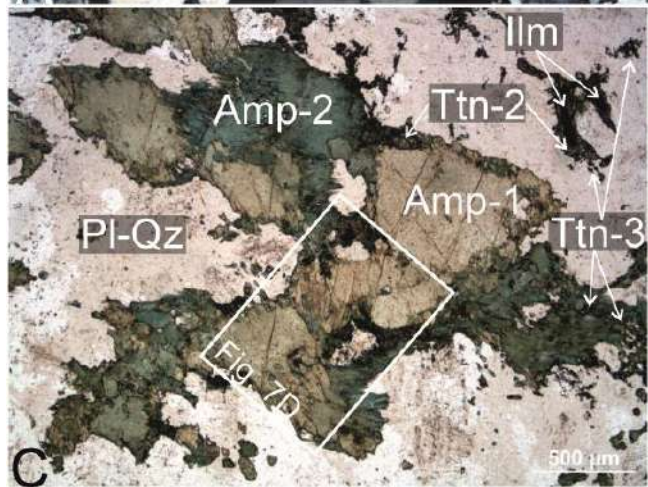
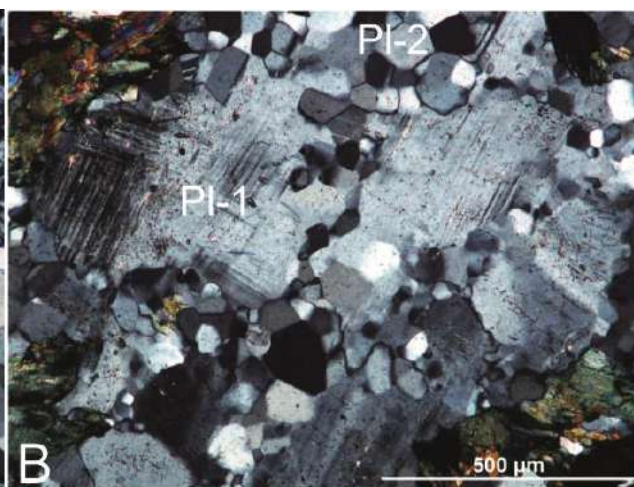
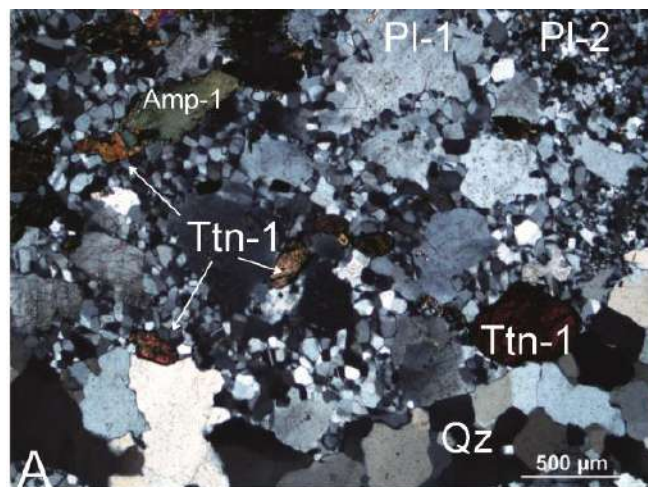


Fig. 7: Magmatic and solid-state textures of the Saleix tonalite observed at the thin section scale (mineral abbreviations after Withney & Evans, 2010). **(a)** Magmatic texture overprinted by syn-metamorphic Pl recrystallization resulting in an inequigranular texture. The magmatic mineralogical assemblage consists in Qz-Pl₁-Amp₁ and large euhedral to subhedral Ttn₁ crystals (sample SAL D2; crossed polars). **(b)** Core-mantle structures in plagioclase resulting from recrystallization of metamorphic Pl₂ by bulging (nucleation and growth of small polygonal grains) from magmatic Pl₁ (sample SAL D2; crossed polars). **(c-d)** Core-mantle structures in amphibole resulting from recrystallization of metamorphic Amp₂₋₃ over magmatic Amp₁ and of metamorphic Ttn₂ over magmatic Ilm. Small Ttn₃ grains occur in the recrystallized Pl₂-Amp₂₋₃ bands (sample SAL E; natural light). **(e)** Magmatic texture overprinted by solid-state fabric (sample SAL E; crossed polars). Note core-mantle structures in Pl, with undulose extinction in magmatic Pl₁ crystals, strained magmatic Amp₁ and preferred orientation of metamorphic Amp₂. **(f)** Magmatic Pl₁ porphyroclasts embedded in the syn-metamorphic Amp₂-Pl₂ shear foliation (sample SAL E; crossed polars). Note dynamic recrystallization of small Pl₂ grains after magmatic Pl₁ porphyroclasts.

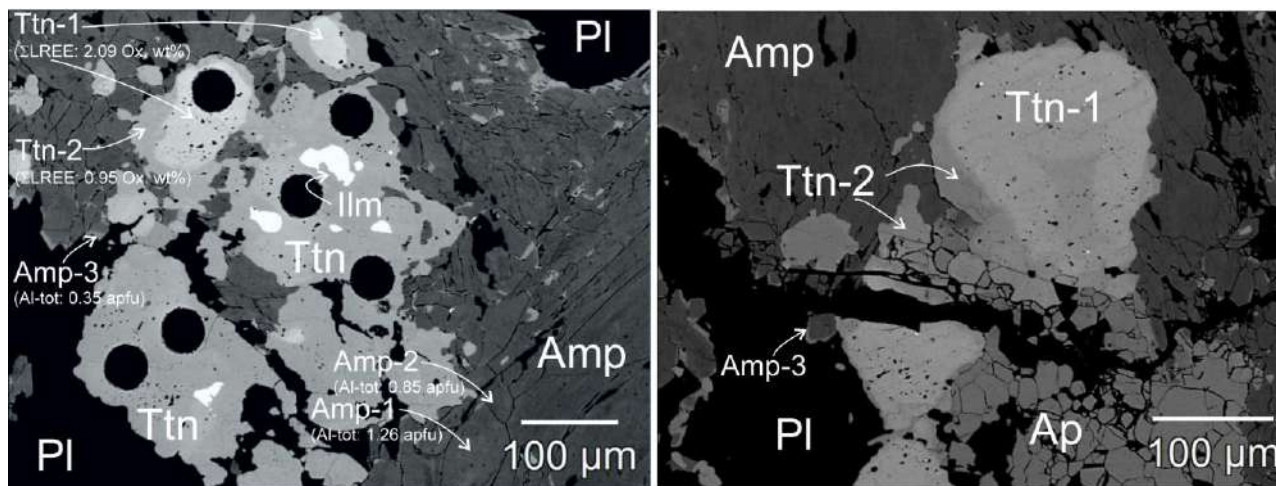


Fig. 8: BSE images showing overgrowth of metamorphic Ttn₂ on magmatic Ilm (a) and Ttn₁ (b; darker rim over brighter core). Note (i) the reduction of REE content when moving from the magmatic Ttn₁ to the metamorphic Ttn₂.

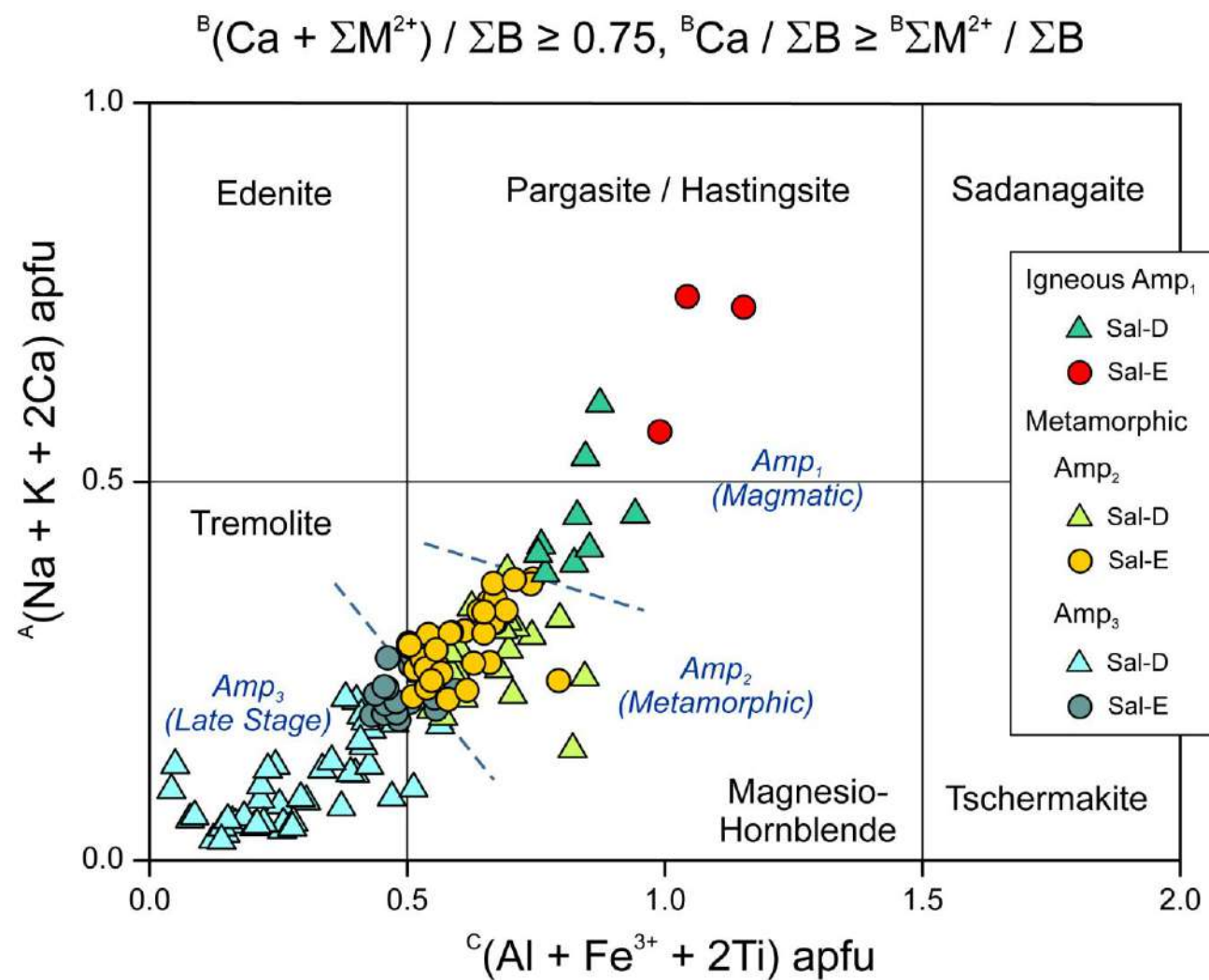


Fig. 9: Composition of Ca-amphiboles in the studied samples. Calcium amphibole names and their compositional boundaries are after Hawthorne et al. (2012).

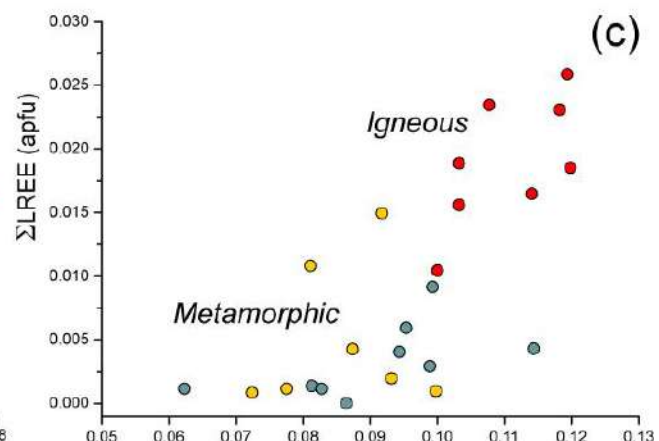
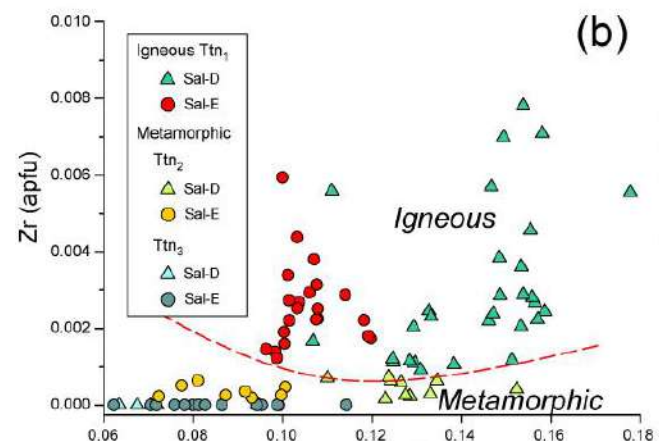
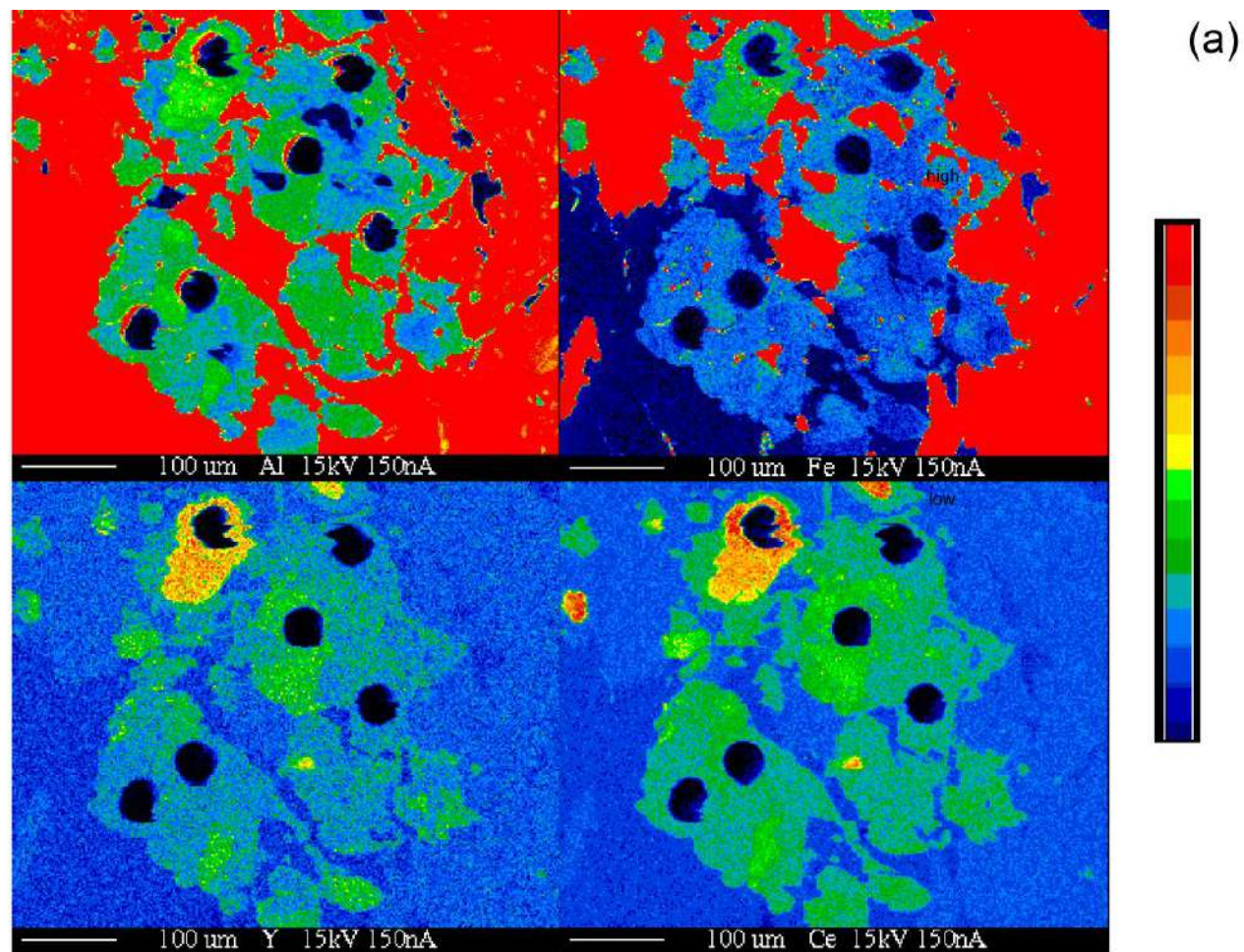


Fig. 10: Titanite chemistry. **(a)** Representative qualitative compositional map showing variations in cation distribution in titanites (cation: Al, Fe, Y, Ce). **(b-c)** EMPA compositional data. The enrichment of Zr and LREE discriminates between magmatic Ttn₁ and mende metamorphic titanites (Ttn₂₋₃).

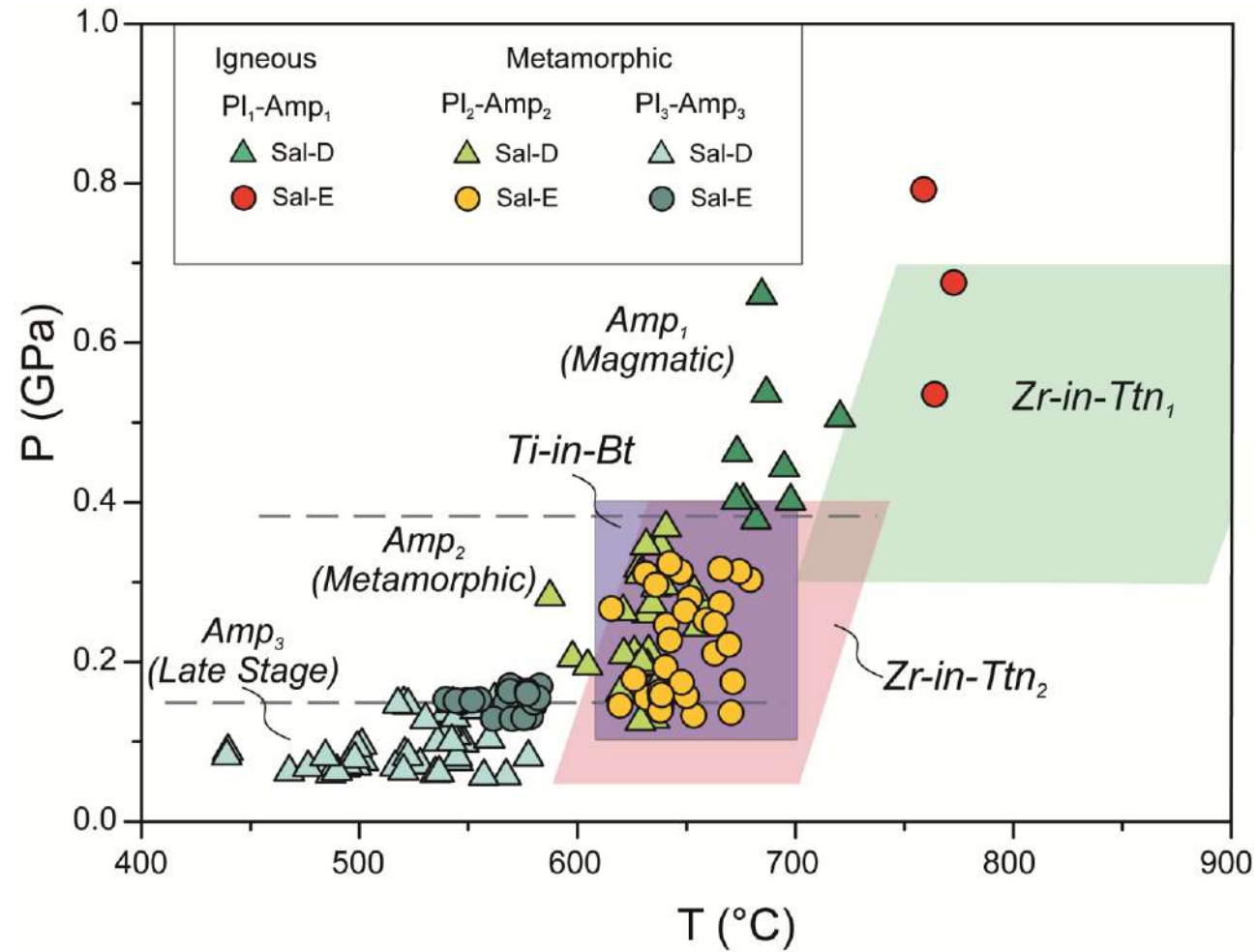


Fig. 11: A summary of the results obtained from thermobarometry models applied to magmatic and metamorphic assemblages from the Saleix tonalites. Green- and pink-shaded fields represent the pressure-temperature domains of crystallization of magmatic (T_{tn1}) and metamorphic (T_{tn2}) titanites, respectively. Blue-shaded field show the results of Ti-in-Bt thermometry. Pressure-temperature fields representative of crystallization of magmatic and metamorphic amphiboles are also indicated in the diagram.

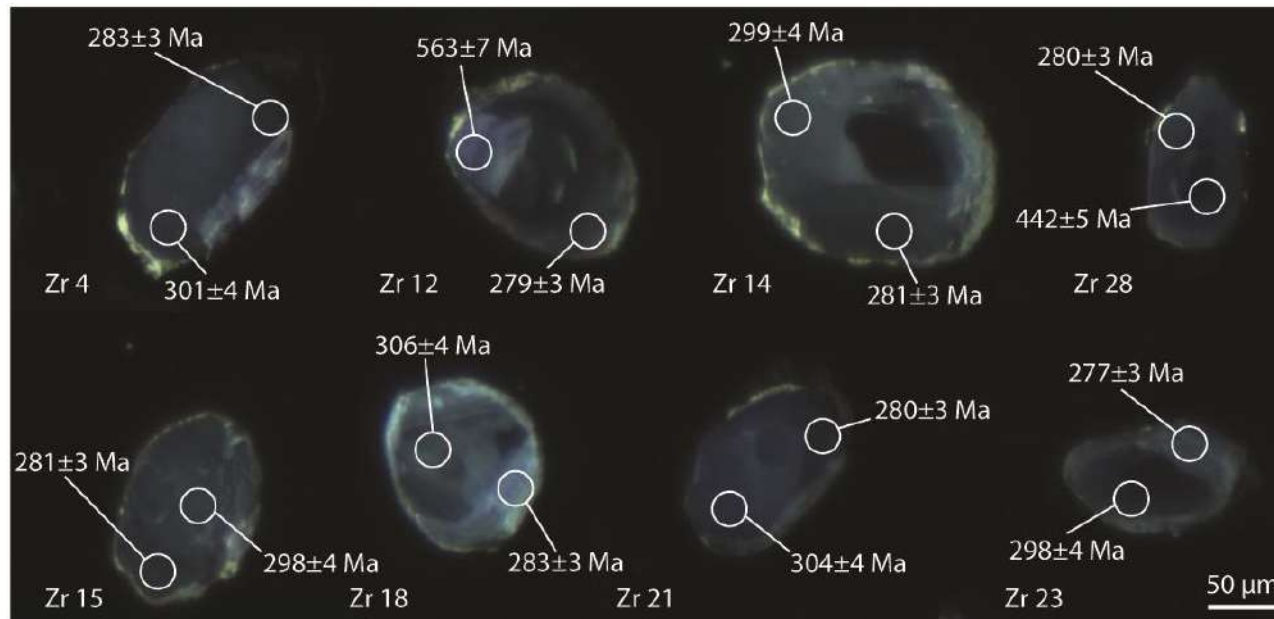


Fig. 12: Representative cathodoluminescence images of the dated zircon grains from the Saleix tonalite (Sample Sal-E). Morphology varies from euhedral to subhedral, with rare anhedral crystals. Zircon crystals dominantly show oscillatory cores with brighter overgrowths at the rims. White circles show the location of LA-ICP-MS spots with the relative $^{206}\text{Pb}/^{238}\text{U}$ ages and their 1σ error (see Table ST8 for details). Note that rim ages are always ~280 Ma.

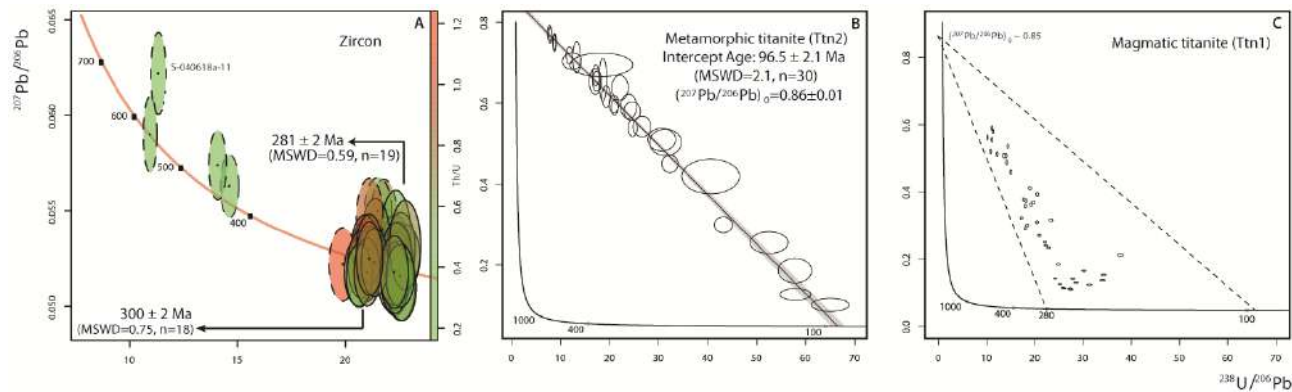


Fig. 13: Tera-Wasserburg diagrams for zircon and titanite U-Pb data (ages are quoted at 2σ absolute). **(a)** Zircon data. All the points are concordant; all the rim ages cluster around $281 \pm 2 \text{ Ma}$ and most of the core ages cluster around $300 \pm 2 \text{ Ma}$. **(b)** Metamorphic Ttn₂ data. All the analytical data are aligned along a discordia line which yields a $(^{207}\text{Pb}/^{206}\text{Pb})_0$ value of 0.86 ± 0.01 and a lower intercept date of $96 \pm 2 \text{ Ma}$ (MSWD=2.1). **(c)** Magmatic Ttn₁ data. All the data are very discordant and plot in a crisis polygon defined by the common Pb composition $(^{207}\text{Pb}/^{206}\text{Pb})_0 = \text{ca } 0.85$, the date yielded by the outer rims of the zircon grains (ca. 281 Ma) and the date yielded by the metamorphic Ttn₂ grains (ca. 96 Ma).

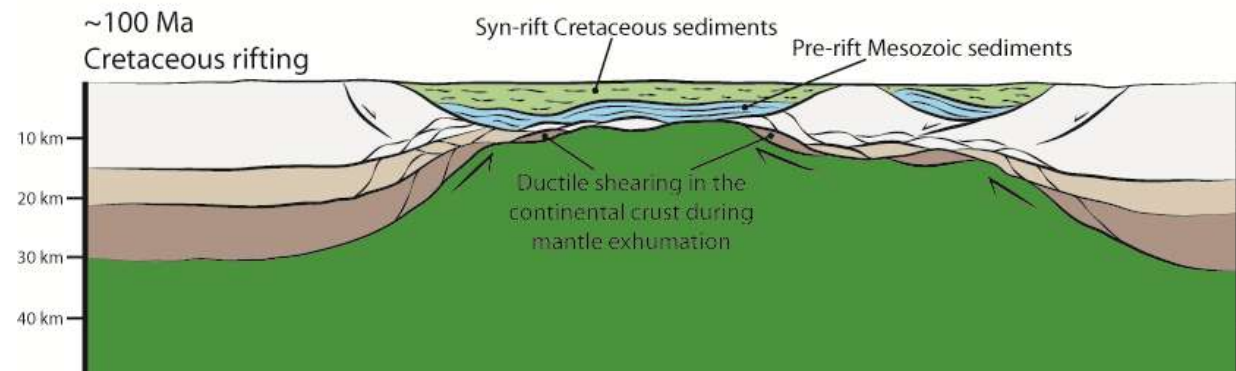
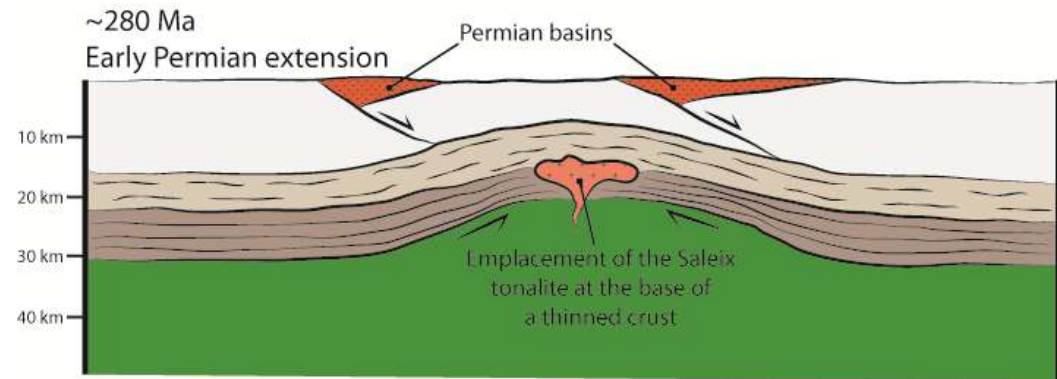
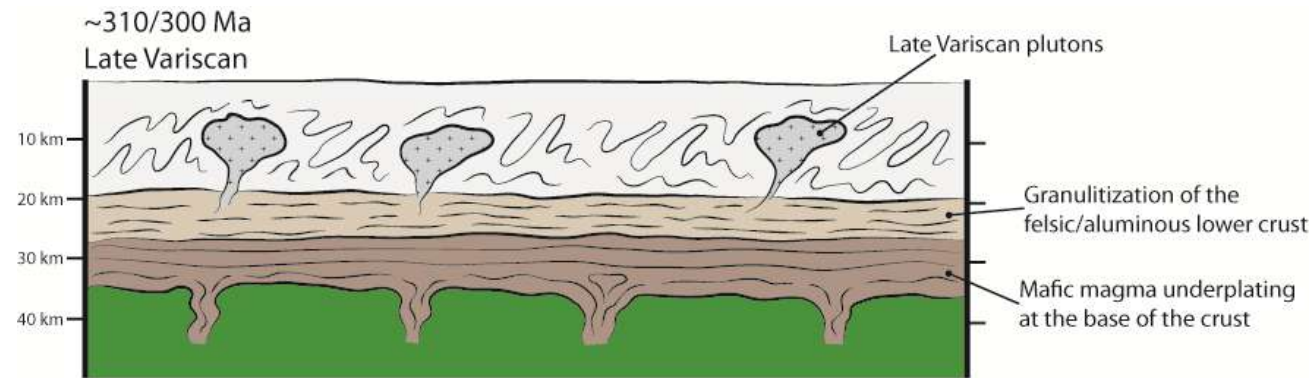


Fig. 14: Conceptual tectonic model for the polyphase evolution of the Variscan continental crust and Cretaceous mantle exhumation in the Pyrenean realm. Towards the end of the Variscan cycle (~310 to ~300 Ma) mafic magma underplating at the base of the crust is synchronous with granulitization and partial melting of the felsic crust and emplacement of gneiss domes in the middle-upper crust. Latest Carboniferous to Early Permian extension (~280 Ma) results in a relevant thinning of the continental crust, as testified by the emplacement of the Saleix tonalite(s) in the lower part of the crust at ~0.5 GPa (i.e. ~18 km). The mid-Cretaceous rifting (~100 Ma) leads to the final exhumation of the sub-continental mantle, solid-state ductile deformation localizes in the continental crust at very shallow depths (~0.2 GPa, i.e. <10 km). The considerable pre-Cretaceous thinning of the continental crust results from the cumulated effects of the extensional events that took place in the Pyrenean realm between the Permian and the Early Cretaceous.

Table 1. List of selected tonalite samples with constituent mineralogy and analytical technique adopted. All samples were collected at site 2 in Fig. 3 (N 42° 46' 56,8'' ; E 01° 24' 29,1'')

Sample	Mineral assemblage	EMPA	Ttn U–(Th)–Pb geochronology	Zrc U–(Th)–Pb geochronology
SAL C	Qz-Pl ⁽¹⁾ -Amp ⁽²⁾ -Kfs-Bt ⁽³⁾ -Ep ⁽⁴⁾ + Ilm + Ttn ⁽⁵⁾ + Zrc + Ap	X		
SAL D1	Qz-Pl ⁽¹⁾ -Amp ⁽²⁾ -Kfs-Bt ⁽³⁾ -Ep ⁽⁴⁾ + Ilm + Ttn ⁽⁵⁾ + Zrc + Ap	X		
SAL D2	Qz-Pl ⁽¹⁾ -Amp ⁽²⁾ -Kfs-Ep ⁽⁴⁾ + Ilm + Ttn ⁽⁵⁾ + Zrc + Ap + Scp	X	X	
SAL E	Qz-Pl ⁽¹⁾ -Amp ⁽²⁾ -Kfs-Ep ⁽⁴⁾ + Ilm + Ttn ⁽⁵⁾ + Zrc + Ap	X	X	X

⁽¹⁾ Including magmatic (Pl₁) and metamorphic (Pl₂) plagioclase

⁽²⁾ Including magmatic (Amp₁) and metamorphic (Amp₂₋₃) amphibole

⁽³⁾ Biotite belongs to the secondary (metamorphic) assemblage

⁽⁴⁾ Including magmatic (Ep₁) and metamorphic (Ep₂) epidote

⁽⁵⁾ Including magmatic (Ttn₁) and metamorphic (Ttn₂₋₃) titanite

Highlights

- Tonalite intrusive(s) emplaced in the lower Pyrenean crust during Early Permian

- The Saleix tonalite(s) emplaced in a partially exhumed lower crust at ca. 281 Ma
- Cretaceous amphibolite facies solid-state fabric overprint Permian magmatic fabric
- Ductile deformation of Saleix Massif occurred at ≤ 10 km depths during Cretaceous
- Pyrenean crustal thinning is polyphase and starts at the end of the Variscan cycle